EXPERIMENTAL AND COMPUTATIONAL STUDY OF GLYCEROL REFORMING OVER WALL-COATED MICROCHANNELS

by

Amin Delparish

B.S., Chemical Engineering, Sharif University of Technology, 2014

Submitted to the Institute for Graduate Studies in
Science and Engineering in partial fulfillment of
the requirements for the degree of
Master of Science

Graduate Program in Chemical Engineering

Boğaziçi University

2017

EXPERIMENTAL AND COMPUTATIONAL STUDY OF GLYCEROL REFORMING OVER WALL-COATED MICROCHANNELS

APPROVED BY:

Prof. Ahmet Kerim Avcı (Thesis Supervisor)	...…….
Prof. Ramazan Yıldırım	...…….
Prof. Ayşe Nilgün Akın	…….

DATE OF APPROVAL: 11.07.2017

ACKNOWLEDGEMENTS

Working under supervision of Prof. Ahmet Kerim Avci was a valuable experience for me. He was not only a patient and incredible mentor but also a teacher with such a friendly approach towards students. This research would not have been possible without his guidance and encouragement. I find myself more than lucky to find the chance to work with him for more than two years.

I would like to acknowledge my thesis committee, Prof. Ramazan Yildirım and Prof. Ayse Nilgun Akin for devoting their valuable time to read and comment on my thesis.

My special thanks goes to lovely current and former members of KB 404: Sinan Koc, Ozgur Yasar Caglar, Pelinsu Bulutoglu, Begum Koca, Hatice Merve Can, Selin Bac and Ayşegül Karakuş.

I have a long list of friends who made my stay at the beautiful Istanbul unforgettable. To name a few, I would mention Seyed Mehdi Emadian, Sina Zare, Sina Ahmadvash, Pouya Yousefi, Farzad Rokhsartalab, Siamak Vajdi, Aidin Sheikhi, Mehdi Madani and Dilara Saadetnejad. Thank you guys for always being there through all my ups and downs.

I devote this thesis to my family. This thesis would not have been possible without their love and encouragement. I am very lucky to have them.

Finally, financial supports provided by TÜBİTAK 1003 – Project No: 113M962 is acknowledged.

ABSTRACT

EXPERIMENTAL AND COMPUTATIONAL STUDY OF GLYCEROL REFORMING OVER WALL-COATED MICROCHANNELS

This study aimed to investigate intensified glycerol reforming both experimentally and computationally. In the experimental part, gas phase oxidative steam reforming (OSR) of glycerol is carried out in an in-house designed microchannel reactor whose inner wall is coated with Rh/Al_2O_3 catalyst. The effects of operating parameters such as reaction temperature, molar inlet carbon-to-oxygen (C/O) and steam-to-carbon (S/C) ratios on glycerol conversion and product distribution are studied. Product analysis is carried out by two online gas chromatographs. The results show that glycerol conversion is enhanced by temperature as the glycerol decomposition is endothermic. Complete glycerol conversion is achieved over the temperature range of 600-700 °C at C/O of 1.125. S/C effect on OSR of glycerol is found to be much less significant as compared to C/O and temperature effects. Conversion and H_2 yield slightly improved with steam content of the feed via WGS and possible coke gasification. It is observed that obtaining a desirable H_2/CO ratio in the product stream, which is found to be in the range of 0.5-1.8, is feasible through changing C/O, S/C and temperature. In the computational part of the work, glycerol steam reforming (SR) is investigated in a heat exchange integrated microchannel reactor by means of mathematical modeling techniques. Heat needed for endothermic glycerol SR taking place in $Co\text{-}Ni/Al_2O_3$ coated channels is supplied by steam flowing in the adjacent channels separated by solid walls. The effects of operational parameters, namely S/C and temperature of the reactive mixture, inlet temperature and velocity of steam, flow configurations of the reactive mixture and steam, and of structural parameters, i.e. reactor wall material and thickness of the wall between the channels on temperature distribution and on glycerol conversion are studied. Product distribution is found to be in alignment with those of experimental studies reported in the literature. The simulation suggests that selectivity towards H_2 is positively correlated with the degree of uniformity of reaction channel temperature, which is also found to dampen undesired CH_4 selectivity.

ÖZET

DUVAR KAPLAMALI MİKRO KANAL ÜZERİNDE GLİSERİN REFORMASYONUNUN DENEYSEL VE BİLİŞİMSEL ÇALIŞMASI

Yapılan bu çalışmanın amacı, gliserin reformasyonunun deneysel ve bilişimsel olarak araştırılmasıdır. Deneysel kısımda, laboratuar koşullarında hazırlanmış ve iç duvarı Rh/Al_2O_3 katalizörü ile kaplanmış mikro kanal reaktöründe, gliserinin oksidatif buhar reformasyonu gaz fazında gerçekleştirilmiştir. Reaksiyon sıcaklığı, reaktör girişindeki karbon-oksijen ve buhar-karbon mol oranlarının, gliserin dönüşümü ve ürün dağılımı üzerindeki etkileri incelenmiştir. Ürün analizi 2 gaz kromatografisi ile yapılmıştır. Gliserin dekompozisyonu endotermik bir reaksiyon olduğundan, gliserin dönüşümünün sıcaklıkla arttığı gözlemlenmiştir. Gliserin dönüşümü, 600-700 °C sıcaklık aralığında ve karbon-oksijen oranının 1.125 olduğu durumda tamamlanmıştır. Buhar-karbon oranı, sıcaklık ve karbon-oksijen oranı ile karşılaştırıldığında, gliserin dönüşümü üzerinde daha az etkili olmuştur. Gliserin dönüşümü ve H_2 verimliliği, girişteki buhar içeriğinin yol açabileceği su gaz kayması ve olası kok gazı ile geliştirilmiştir. Yapılan çalışmalar sonucu H_2/CO oranı 0.5-1.8 aralığında bulunmuş olup, istenilen H_2/CO oranını elde etmenin, karbon-oksijen ve buhar-karbon oranları ve sıcaklık değiştirilerek mümkün olabileceği gözlemlenmiştir. Çalışmanın bilişimsel kısmında, gliserin dönüşümü ısı değişim üniteli, duvarı ayrılmış, dikdörtgen şeklinde, paralel reaksiyon ve ısıtma kanalları içeren mikro kanal reaktöründe, matematiksel modelleme teknikleri vasıtasıyla incelenmiştir. $Co\text{-}Ni/Al_2O_3$ katalizörü ile kaplanmış kanallarda gerçekleşen ve endotermik olan gliserin dönüşümü için gereken ısı, duvarlarla ayrılmış bitişik kanallar üzerinden geçen buhar ile sağlanmıştır. Reaktif karışımın buhar-karbon oranı ve sıcaklığı, giriş sıcaklığı ve buhar hızı ile reaktif karışım ve buhar akış konfigürasyonları, ve reaktör duvar materyali ile reaksiyon ve ısıtma kanalları arasındaki duvar kalınlığı gibi değişkenlerin, sıcaklık dağılımı ve gliserin dönüşümü üzerindeki etkisi araştırılmıştır. Ürün dağılımı, literatürde yapılan deneysel çalışmaların sonucuyla paralel bulunmuştur. Simülasyon sonuçları, reaksiyon kanal sıcaklığının homojen dağılımının istenmeyen CH_4 seçiciliğini azaltmasının yanı sıra H_2 üretimini pozitif etkilediğini göstermektedir.

TABLE OF CONTENTS

ACKNOWLEDGEMENTS iii
ABSTRACT iv
ÖZET v
LIST OF FIGURES viii
LIST OF TABLES xi
LIST OF SYMBOLS xii
LIST OF ACRONYMS/ABBREVIATIONS xiv
1. INTRODUCTION 1
2. LITERATURE SURVEY 4
2.1. Ethanol Reforming in Intensified Catalytic Reactors 4
2.2. Dimethyl Ether Reforming in Intensified Catalytic Reactors 7
2.3. Ethylene Glycol Reforming in Intensified Catalytic Reactors 10
2.4. Glycerol Reforming in Intensified Catalytic Reactors 11
3. EXPERIMENTAL WORK 16
3.1. Materials 16
3.2. Experimental Systems 17
3.2.1. Catalyst Preparation System 17
3.2.2. Catalytic Reaction System 18
3.2.3. Product Analysis System 20
3.3. Catalyst Preparation and Pretreatment 24
3.3.1. Preparation of Support 24
3.3.2. Preparation of Active Catalysts 24
3.3.4. Catalyst Coating on Microchannel Plates and Pretreatment 25
3.4. Reaction Tests 25
4. MODELING AND SIMULATION 27
4.1. Description of the Microchannel Reactor, Model Equations and Assumptions 27
4.2. Kinetic Model 31
4.3. Numerical Solution 33
5. RESULTS AND DISCUSSION 35

5.1. Oxidative Steam Reforming of Glycerol in a Catalytic Microchannel 35
5.1.1. Effect of Temperature on Glycerol Oxidative Steam Reforming 35
5.1.2. Effect of C/O on Glycerol Oxidative Steam Reforming 38
5.1.3. Effect of S/C on Glycerol Oxidative Steam Reforming 40
5.2. Modeling of Glycerol Steam Reforming in a Heat-Exchange Integrated Microchannel Reactor 43
5.2.1. Effect of S/C 43
5.2.2. Effect of Flow Configuration 45
5.2.3. Effects of Inlet Temperatures of Reactive Mixture and Steam 46
5.2.4. Effect of Inlet Steam Velocity 49
5.2.5. Effect of Reactor Material and Thickness of the Wall Separating Channels. 50
6. CONCLUSIONS AND RECOMMENDATIONS 56
6.1. Conclusions 56
6.1.1. Experimental Part Conclusions 56
6.1.2. Computational Part Conclusions 56
6.2. Recommendations 57
REFERENCES 58
APPENDIX A: CALIBRATION OF THE GAS CHROMATOGRAPHS 72

LIST OF FIGURES

Figure 3.1. The Impregnation System: 1. Ultrasonic Mixer 2. Buchner Flask 3. Vacuum Pump 4. Peristaltic Pump 5.Aqueous Catalyst Solution 6. Silicon Tubing. …… 17

Figure 3.2. Feed Section of Glycerol Reforming System. …..…..……. 18

Figure 3.3. Furnace and Reaction Section of Glycerol Reforming System. …..… 19

Figure 3.4. Post-reaction Section of Glycerol Reforming System. ……..…..... 20

Figure 3.5. Gas Chromatographs Used in Glycerol Reforming System. ..…….… 21

Figure 3.6. Schematic Diagram of the Reaction System. …….……....……. 23

Figure 3.7. Microreactor Configuration a. Coated Microchannel Reactor b. Location of Steel Housing in Quartz Tube. …….……..... 26

Figure 4.1. Heat-exchange integrated microchannel reactor and the unit cell (channel dimensions are not to scale). ……..……... 29

Figure 5.1. Temperature effect on glycerol OSR. ……..... 37

Figure 5.2. Effect of temperature on outlet H_2/CO ratio. …….....…….... 37

Figure 5.3. Effect of C/O on glycerol OSR at 550 °C. ……....…….... 39

Figure 5.4. Effect of C/O on glycerol OSR at 700 °C. …….…..... 39

Figure 5.5. Effect of C/O on outlet H_2/CO ratio. ……... 40

Figure 5.6. Effect of S/C on glycerol OSR at 550 °C. ……..…… 41

Figure 5.7. Effect of S/C on glycerol OSR at 700 °C. ……..…. 42

Figure 5.8. Effect of S/C on outlet H_2/CO ratio. ……...……...…. 42

Figure 5.9. Effect of S/C on the selectivities towards H_2, CO_2, CO and CH_4. ….. 44

Figure 5.10. Parity plot for product selectivities at 823 K and S/C between 1.14 and 3.98. ……..……. 44

Figure 5.11. Effects of flow direction of steam and absence of steam heating on temperature of the reforming channel. ……...…….……. 46

Figure 5.12. Effect of the inlet temperature of the glycerol vapor/steam mixture on temperature of the reforming channel. Simulated values of inlet temperature of the reactive mixture are presented in the figure. ……. 47

Figure 5.13. Effect of inlet temperature of steam on temperature of the reforming channel. Simulated values of inlet temperature of steam are presented in the figure. …….……...……. 48

Figure 5.14. Effect of inlet velocity of steam on temperature of the reforming channel. Simulated values of steam inlet velocity are presented in the figure. ……... 49

Figure 5.15. Effect of thickness of the wall separating reforming and heating channels on temperature of the reforming channel. Simulated wall thickness values are presented in the figure. ……..……...……... 51

Figure 5.16. Effect of solid wall material on temperature of the reforming channel. Simulated wall materials are mentioned in the figure. ….... 52

Figure A.1. Calibration Curve for N_2. ……..……...……..... 72

Figure A.2. Calibration Curve for H_2. ……..……...……..... 72

Figure A.3. Calibration Curve for CH_4. ……..……...……..... 73

Figure A.4. Calibration Curve for CO. ……..……...……..….. 73

Figure A.5. Calibration Curve for CO_2. ……..……...……..….. 74

Figure A.6. Calibration Curve for C_2H_4. ……..……...……... 74

Figure A.7. Calibration Curve for C_2H_6. ……..……...……..... 75

LIST OF TABLES

Table 3.1. Chemicals used in catalyst preparation. 16

Table 3.2. GC conditions for product gas analysis. ……..... 22

Table 4.1. Model equations in 2D cartesian coordinates. ……..... 28

Table 4.2. Correlations used to predict physical properties of the reactive mixture and porous catalyst layer……..……..... 30

Table 4.3. Kinetic parameters for the glycerol, CO_2 and CH_4 consumption/generation. 32

Table 4.4. Investigated parameters and their respective range/attribute. …….. 34

Table 5.1. Product yields over 550-700 °C range at C/O 1.125 and S/C of 5. 36

Table 5.2. Product yields over C/O range of 0.75-2.25 at S/C of 5 and two temperatures (550 °C and 700 °C). …….. 38

Table 5.3. Product yields over S/C range of 3-5 at C/O of 1.125 and two temperatures (550 °C and 700 °C). ……..... 40

Table 5.4. Glycerol conversions obtained at different structural and operational configurations; default values of the parameters are shown in italics. ... 54

LIST OF SYMBOLS

A	pre-exponential factor, $mol.m^{-2}.s^{-1}.kPa^{-(\beta+\gamma)}$
A_{metal}	metal surface area of the catalyst, $m^2.kg_{cat}^{-1}$
C_2	inertial resistance coefficient of the washcoat, m^{-1}
$c_{p,i}$	heat capacity of species *i*, $J.kg^{-1}.K^{-1}$
$c_{p,m}$	heat capacity of gas mixture, $J.kg^{-1}.K^{-1}$
$D_{eff,i,m}$	effective diffusivity of species *i* in the mixture, $m^2.s^{-1}$
D_{ij}	binary diffusion coefficient, $m^2.s^{-1}$
$D_{i,m}$	diffusivity of species *i* in the mixture, $m^2.s^{-1}$
$D_{K,i}$	Knudsen diffusion coefficient of species *i*, $m^2.s^{-1}$
d_p	catalyst particle diameter, m
d_{pore}	average pore diameter, m
E_A	activation energy, $J.mol^{-1}$
$\vec{\mathbf{F}}$	momentum source/sink term, $kg.m^{-2}.s^{-2}$
F_i	molar flux of species *i*, $mol.m^{-2}.s^{-1}$
$\mathbf{I}$	3×3 identity matrix, –
$\vec{J}_i$	diffusive mass flux of species i, $kg.m^{-2}.s^{-1}$
k_{cat}	thermal conductivity of the catalytic washcoat layer, $W.m^{-1}.K^{-1}$
$k_{eff,m}$	effective thermal conductivity of gas mixture in washcoat layer, $W.m^{-1}.K^{-1}$
k_i	thermal conductivity of species *i*, $W.m^{-1}.K^{-1}$
k_m	thermal conductivity of gas mixture, $W.m^{-1}.K^{-1}$
k_w	thermal conductivity of the solid wall, $W.m^{-1}.K^{-1}$
L	length of the unit cell, m
M_i	molecular weight of species *i*, $kg.mol^{-1}$
M_m	average molecular weight of gas mixture, $kg.mol^{-1}$
N_g	number of gas-phase species

p_i	partial pressure of species *i*, kPa
p	total pressure, kPa
r_{rxn}	rate of reaction (*rxn* = DEC, WGS or MET), mol.kg_{cat}^{-1}.s^{-1}
R	gas constant (= 8.314 J.mol^{-1}.K^{-1})
R_i	consumption/generation rate of species *i*, mol.kg_{cat}^{-1}.s^{-1}
S_{BET}	BET surface area of the catalyst, m^2. kg_{cat}^{-1}
S_i	selectivity towards species *i*, %
T	temperature, K
$\vec{\mathbf{v}}$	velocity vector, m.s^{-1}
V_{pore}	catalyst pore volume, m^3.kg_{cat}^{-1}
x, y, z	cartesian coordinates
y_i	mole fraction of species *i*, –
Y_i	mass fraction of species *i*, –
α	permeability of the washcoat, m^2
β	partial reaction order for glycerol, –
ΔH^o	standard enthalpy of reaction, kJ.mol^{-1}
ΔH_{rxn}	enthalpy of reaction (*rxn* = DEC, WGS or MET), kJ.mol^{-1}
ε_{cat}	porosity of the washcoat layer, –
Φ_{ij}	dimensionless parameter for the mixture of *i* and *j*, –
γ	partial reaction order for steam, –
μ_i	viscosity of species *i*, kg.m^{-1}.s^{-1}
μ_m	average gas mixture viscosity, kg.m^{-1}.s^{-1}
ρ_{cat}	density of the catalytic washcoat, kg.m^{-3}
ρ_m	density of gas mixture, kg.m^{-3}
υ_i	unitary constant that indicates if *i* is consumed or produced, –
$(\sum \upsilon)_i$	sum of the atomic diffusion volumes for species *i*, –
τ_{cat}	catalyst tortuosity, –

LIST OF ACRONYMS/ABBREVIATIONS

cat	catalyst
DEC	glycerol decomposition reaction
eff	effective
i, j	species indices
in	channel inlet
MET	methanation reaction
OSR	oxidative steam reforming
out	channel outlet
rxn	reaction
SR	steam reforming
S/C	steam-to-carbon molar ratio at the inlet
w	solid wall phase
WGS	water-gas shift reaction

1. INTRODUCTION

Increasing environmental concerns about the conventional fossil fuels and their monotonically elevating cost of exploration and production have accelerated efforts towards finding renewable and widely available alternatives. Among several options, biodiesel is attracting interest as it is carbon neutral and can successfully mimic the crude-oil based diesel [1, 2]. Production of biodiesel is conventionally carried out by transesterification of animal-based or vegetable oils with methanol (or ethanol). In this process, one mole of glycerol is produced for every three moles of biodiesel, corresponding to the presence of ca. 10% of glycerol by weight in the reaction mixture [1, 2]. This stoichiometry, however, causes undesirably high supply of glycerol: it is predicted that there will be three megatons of glycerol production by 2020, whereas the amount of glycerol consumption in commercial applications is expected to remain below five hundred kilotons [3]. This issue calls for the need of efficient conversion of excess glycerol into value added products such as H_2 and syngas, which are key components employed in critical petroleum refining operations such as hydrocracking and hydrotreating, as well as in Fischer-Tropsch synthesis for producing hydrocarbons [4].

Steam reforming (SR) is the conventional technique for converting hydrocarbons into a H_2-rich mixture. The process involves reaction of the hydrocarbon molecule with steam at temperatures in excess of ~800 K over a conventional fixed-bed reactor (FBR). Glycerol SR (Reaction 1.1) is a combination of its decomposition (DEC) (Reaction 1.2) and water-gas shift (WGS) (Reaction 1.3) [5]:

$$C_3H_8O_3 + 3H_2O \rightarrow 3CO_2 + 7H_2, \ \Delta H° = 128 \text{ kJ mol}^{-1} \quad (1.1)$$

$$C_3H_8O_3 \rightarrow 3CO + 4H_2, \ \Delta H° = 251 \text{ kJ mol}^{-1} \quad (1.2)$$

$$CO + H_2O \rightarrow CO_2 + H_2, \ \Delta H° = -41 \text{ kJ mol}^{-1} \quad (1.3)$$

In addition to SR, glycerol conversion is applicable through partial oxidation (POX) whose efficiency depends directly on controlling the amount of introduced oxygen. Reaction 4 represents the global POX of glycerol:

$$C_3H_8O_3 + (3/2)O_2 \rightarrow 3CO_2 + 4H_2,\ \Delta H° = -598\ kJ\ mol^{-1} \quad (1.4)$$

Oxidative steam reforming (OSR) is an alternative efficient process of glycerol conversion that is obtained by combining POX and SR. This process has certain advantages over SR, specifically in terms of energy saving and coke reduction; however, it has been given less interest [6]. OSR is described as follows:

$$C_3H_8O_3 + (3/2\text{-}y)H_2O + (3/4\text{-}x)O_2 \rightarrow (2x+y)CO + (3\text{-}(2x+y))CO_2 + (5.5\text{-}y)H_2 \quad (1.5)$$

By adjusting the amount of introduced O_2 and steam, the process would provide syngas with desired H_2/CO ratio, which is an important metric to quantify the quality of synthesis gas [3]. This strategy also forms the basis of autothermal reforming (ATR) which combines exothermic homogeneous oxidation of the part of the hydrocarbon to provide heat needed to drive SR of the remaining fuel and to adjust the WGS equilibrium for producing synthesis gas [7, 8].

Efficiency of SR and OSR depends strongly on the degree of heat transfer along the bed of catalyst particles in the reactor. However, in case of glycerol reforming, most of the studies are focused on developing catalysts that can deliver elevated conversions at reduced temperatures (i.e. with less external heat supply) with minimal carbon formation. Among the investigated catalysts are Ni, Co and noble metals such as Rh, Pt and Ru supported over different supports including Al_2O_3, CeO_2 and ZrO_2 in particulate form within FBRs [3]. Owing to the inherent weakness FBRs in terms of heat transfer, heat supply to the reactors is adjusted to guarantee the desired conversion and throughput. As a result of the additional heating requirements, release of the natural gas combustion products such as CO_2 and nitrogen oxides becomes more significant. At this point, intensified reactors such as microchannel, monolith or foam reactors become important, as these units offer surface area-to volume ratios that are up to two orders of magnitude higher than those of conventional units like FBRs [9-11]. When this property is accompanied by the use of reactor or catalyst support materials with high thermal conductivities, the resistance against heat flow can be decreased significantly within the reactor, allowing near isothermal operation of the catalyst bed with reduced external heat transfer requirements. As a result, it becomes possible to operate the reactor at a strictly

controlled, narrow temperature interval in which the catalyst bed delivers the best performance in terms of activity, selectivity and stability with less emissions associated with external heating/cooling duties. Improved surface areas in compact volumes also increase void space in the reactor and reduce pressure drop, an important operational constraint in commercial practice. Apart from their superior heat transfer and pressure drop properties, narrow residence time distribution characteristics of structured intensified reactors promote carrying out the aforementioned processes with targeted product selectivities.

This study is consisted of two separate parts investigating glycerol reforming both experimentally and computationally. In the experimental part, a parametric study of glycerol OSR over a Rh based catalyst is conducted. The investigated parameters are reaction temperature, molar inlet carbon-to-oxygen and steam-to-carbon ratios (C/O and S/C, respectively) and reactant dosing configuration. The computational study, on the other hand, is aimed to provide a deep and systematic insight into the role of heat transfer in the micro-scale on glycerol SR. In this context, SR of glycerol in a heat exchange integrated microchannel reactor is investigated by means of a mathematical model-based parametric study.

This work is composed of six chapters. In Chapter 2, a literature survey about intensified catalytic reactors for reforming of renewable fuels to hydrogen and synthesis gas is presented. A detailed explanation of experimental set-up, methods and procedures for catalyst preparation and catalytic activity tests are presented in Chapter 3. Simulation studies of glycerol SR are described in Chapter 4 by providing an explanation of the mathematical model and related numerical solution techniques. Results and discussion of both experimental and computational work are presented in Chapter 5. Chapter 6 includes major conclusions and recommendations for the future studies.

2. LITERATURE SURVEY

Intensified reactors have operating capacities and compact volumes that are highly compatible with decentralized or space-limited operations aiming the valorization of renewable fuel(s) available on the production site into H_2 and synthesis gas. Increasing popularity of such applications that offers sustainable, clean, efficient catalytic operation with high selectivity towards desired products has set path to the evolution of a significant number of research studies. Recent studies and advances about catalytic conversion of a set of renewable fuels, namely ethanol, dimethyl ether, ethylene glycol and glycerol into H_2 and synthesis gas in monolith, microchannel and foam reactors are reviewed in the following sections.

2.1. Ethanol Reforming in Intensified Catalytic Reactors

Among a number of renewable fuels, ethanol is considered to be advantageous due to its high energy density, low volatility, non-toxicity, easy delivery, safe storage and availability [12-14]. Ethanol can be economically produced from anaerobic fermentation of abundant biomass materials such as starch-rich materials or lignocellulosic feedstocks [14, 15]. Reforming of ethanol to H_2 and synthesis gas has been studied widely in diverse catalytic systems employing catalysts based on both noble metals (Pd [16], Rh [17], Ru [18]) and non-noble ones (Co [19], Ni [20], Cu [21]) over various supports.

Andreev *et al.* [22] compared the activity of Co/ZnO and Rh/Al_2O_3 catalysts for ethanol SR in a microchannel reactor. At H_2O/C_2H_5OH of 10 and 973 K, they obtained H_2 yields of 7.6×10^3 and 2.6×10^4 $mL.g_{cat}^{-1}.h^{-1}$ over Co/ZnO and Rh/Al_2O_3, respectively. Rh-based catalyst exhibited lower selectivity towards CH_4 and CO_2. Co/ZnO was found to be strongly coked due the formation of a large number of carbon fibers, whereas no carbon deposition was observed over Rh/Al_2O_3. The microchannel reactor showed a specific H_2 yield that was almost two times higher than that of a traditional fixed-bed tubular reactor. Dominguez *et al.* [23] reported 100% ethanol conversion and H_2 yield of 97% at steam-to-

carbon molar ratio (S/C) of 3, 648 K and space velocity of 120 mol g_{cat}^{-1} h^{-1} over cobalt talc ($Co_3[Si_2O_5]_2(OH)_2$) loaded microchannels. Uriz *et al.* [24] implemented a kinetic model into the computational fluid dynamics (CFD) codes to describe ethanol SR in a Co/ZnO coated microchannel. At temperatures above 898 K and gas hourly space velocities (GHSV) up to 7.0×10^4 h^{-1} H_2 yield of 70% and CO selectivity of 25% were obtained. Nearly isothermal conditions were achieved in the microchannels with characteristic dimensions below 3.5×10^{-4} m.

Men *et al.* [25] investigated Rh, Ru, Ni and Co active metals and Al_2O_3, CeO_2, SiO_2, ZnO and MgO supports and promoters for ethanol SR. Rh/Al_2O_3 was found to be the most active monometallic catalyst in the temperature range of 673-873 K. Formation of significant amounts of acetaldehyde and ethylene in the microchannels suggested that ethanol dehydrogenation was the dominant reaction at 673 K. However, the extent of ethanol SR was notable above 773 K, since a rapid increase of ethanol conversion and selectivities towards CO and H_2 was observed. The authors also reported that addition of Ni and CeO_2 could vastly suppress the dehydration pathway, as significant reductions in selectivities towards acetaldehyde (from 20.1 to 6.2%) and ethylene (from 59.1 to 0%) were reported at 673 K. Gorke *et al.* [26] observed complete ethanol conversion at temperatures above 823 K under SR conditions using microchannels coated with Rh/CeO_2. At temperatures in excess of 898 K, a H_2 space time yield of 24 mol g_{cat}^{-1} h^{-1} was reached at S/C of 2 and a residence time of 11 ms. Even at S/C ratios below 2, negligible coke formation was observed due to the low acidity of the applied catalyst and absence of heat transfer resistance in the catalyst layer. Rahman *et al.* [27] developed a catalytic hollow fibre microreactor (CHFMR) in which $Ni/MgO\text{-}CeO_2$ was impregnated into finger-like structure YSZ hollow fibres operating as a hundreds of conical microchannels. CHFMR enabled direct scale-up and, due to the better catalyst utilization, reduced the required catalyst mass up to 80% compared to a fixed bed reactor. Using 8 units of CHFMRs containing 1.8×10^{-2} g of the catalyst, a H_2 production rate of 540 mL h^{-1} was achieved from ethanol SR at 780 K with 3.7×10^{-3} mol h^{-1} ethanol flow rate at H_2O/C_2H_5OH of 5.

Peela *et al.* [28] studied ethanol OSR over Rh/Al_2O_3 catalysts in a microchannel reactor and found that addition of ceria could significantly increase the activity and selectivity towards H_2 and CO. The best performance, i.e. complete ethanol conversion, H_2

selectivity of 3.5 mol_{H2} $mol_{ethanol}^{-1}$ and CO selectivity of 0.2 mol_{CO} $mol_{ethanol}^{-1}$ was observed at 823 K and O_2/C_2H_5OH of 0.5 over Rh/Al_2O_3-CeO_2. The catalyst was slightly more selective towards syngas under SR conditions, but OSR resulted in higher activity and less coke formation. H_2 yield obtained in OSR was ~11.2×10^4 $mL.g_{cat}^{-1}.h^{-1}$, while it was ~12.8×10^4 $mL.g_{cat}^{-1}.h^{-1}$ in SR which was 3 times higher than that reported by Cai *et al.* [29]. Peela *et al.* [30] also reported that adding Ni to Rh/CeO_2-Al_2O_3 was detrimental to the catalyst performance due to decreased reducibility and formation of a Ni layer over Rh sites. The same authors showed that ethanol SR on Rh/CeO_2-Al_2O_3 can be described by a reaction scheme consisting of reaction between steam and ethanol, decomposition of ethanol, methane SR and WGS [31]. From simulation results it was revealed that almost homogenous temperature profiles together with complete ethanol conversion were achievable in a coupled reactor/heat-exchange co-current system used in SR [31]. Bruschi *et al.* [32] found that at low inlet temperatures, counter-current flow configuration was preferable, while, in the case of preheated feed, the co-current scheme provided more favorable temperature profiles. Considering the fact that the optimal heat flux for ethanol SR was decreasing, Anzola *et al.* [33] demonstrated that with inlet temperature of 873 K at the reaction side, co-current flow configuration would be a much better choice, especially in the case of channel widths below 7.0×10^{-4} m.

Divins *et al.* [34] presented a silicon micromonolith reactor containing 1.5×10^6 regular channels each of which had a diameter of 3.3×10^{-6} m and coated with $Rh\text{-}Pd/CeO_2$ catalyst. Complete SR conversions of ethanol were obtained for all the GHSVs tested in the range of 2.1×10^5 h^{-1} to 1.3×10^6 h^{-1} at 873 K and S/C = 3. However, due to the formation of acetaldehyde, H_2 yield decreased from 0.65 to 0.53 with increasing GHSV. Acetaldehyde was not was detected under OSR conditions at which H_2 yield was found to diminish. Nevertheless, the demand on external energy was significantly reduced when O_2 was fed together with ethanol and steam. The authors also reported that normalized activity values for the silicon micromonolith were about 2 orders of magnitude higher in comparison with conventional cordierite monoliths. Llorca *et al.* [35] applied a micromonolithic support with $>10^6$ parallel, 3.3×10^{-6} m diameter microchannels coated with Co_3O_4-ZnO catalyst to the SR of ethanol. They reported that a specific inner surface of 10^5-10^6 m^2 m^{-3} was obtained using a complexation-decomposition coating method. At S/C of 3, GHSV of 2.0×10^4 h^{-1} and temperature of 773 K, stable selectivities of ~67%

towards H_2 and 14% towards CO were obtained. Casanovas *et al.* [36] compared silicon micromonoliths (channel diameter of 3-4×10^{-6} m) with conventional monoliths (channel width of 9.0×10^{-4} m) and semicylindrical microchannels (3.5×10^{-4} m radius). All the reactors were coated with Co_3O_4 catalyst and tested in ethanol SR. An increase in specific H_2 production of about 1 order of magnitude was reported when monolith was replaced by microreactor and of 1-2 orders of magnitude when microreactor was replaced by silicon micromonolith. As the comparison was done at three different temperatures, Tilland *et al.* [37] carried out a simulation study under identical working conditions confirming the experimental results reported by Casanovas *et al.* [36]. The outstanding enhancement achieved in the specific surface area (from 2.2×10^3 m^2 m^{-3} for the monoliths to 3.5×10^5 m^2 m^{-3} for the micromonoliths) and the catalyst amount per unit of reactor volume appeared to be the main reasons for the observed increase in reactor performance [36, 37]. Lopez *et al.* [38] also reported tremendous advantages of increasing the geometric area per unit volume. They fabricated a micromonolithic substrate with 4×10^6 channels/cm^2 and channel diameter equal to 3.3×10^{-6} m through a photoassisted electrochemical etching method. The operating parameters including temperature (673-773 K), feed concentration (S/C = 1.5-6.5) and residence time (0.03–0.9 s) were monitored to find the optimum conditions. Over Co_3O_4-ZnO catalyst, ethanol conversion of 87.3% and H_2 selectivity of 60% were obtained at S/C of 3, residence time of 0.44 s and temperature of 773 K. Pla *et al.* [39] also fabricated a micromonolithic reformer containing 2×10^4 silicon microchannels per cm^2 with a channel diameter of 5.0×10^{-5} m yielding a specific surface area of 3.2×10^3 m^2 m^{-3}. H_2 selectivity of ~56%, CO selectivity of ~27% and H_2 yield of 35% were obtained over Rh-Pd/CeO_2 catalyst in ethanol SR at 1023 K.

2.2. Dimethyl Ether Reforming in Intensified Catalytic Reactors

Dimethyl ether (DME) is considered as a clean fuel for the 21st century, as it burns without particulate matter and sulfur oxides emissions [40, 41]. DME has gained much attention as a fuel that can be derived from biomass, with intrinsic merits such as non-carcinogenicity, high H/C ratio, storage and handling characteristics similar to those of liquid petroleum gas [41, 42]. Low reforming temperatures compared to those involved in ethanol and methanol, together with less coke formation due to the lack of the C-C bond make DME a promising candidate for on-board conversion to H_2 [43, 44].

Mihai *et al.* [45] subjected Pt/Al_2O_3 washcoated monolith to sulfur aging. Even though only a minor effect on catalyst activity was reported, a significant amount of methanol was formed. However, thermal aging of Pt/Al_2O_3 at 1073 K did not have a notable effect on catalyst performance. Ledesma *et al.* [46] evaluated the performance of various Pd impregnated supports coated onto monoliths in SR of DME. The experiments were conducted at S/C of 1.5, temperature of 473-823 K and GHSV of 1.5×10^3 h^{-1}. Pd/ZrO_2 turned out to yield the highest H_2 and the lowest CH_4, as compared to the other tested Pd loaded supports including CeO_2, CeO_2-ZrO_2, MnO_2, SnO_2, Al_2O_3, WO_3 and WO_3-ZrO_2. Complete DME conversion and a H_2 yield of ~55% was reported over Pd/ZrO_2 at temperature of 823 K. As no clear correlation between H_2 yield and support acidity or Pd dispersion was observed, the authors supposed that the interaction between metal particles and the support might have dictated the catalyst performance. It was reported that the reaction was probably initiated via dissociative adsorption of DME into methoxy species, which was similar to the mechanism proposed by Kruger *et al.* [47] for ATR over Rh based catalyst. The reaction of methoxy species with hydroxyl groups resulted in formation of formate and carbonate species which were assumed to be desorbed as H_2, CO_2, CO and CH_4. Ledesma *et al.* [48-51] also examined the catalytic monoliths loaded with Cu, Zn, or Cu-Zn supported on ZrO_2, CeO_2 or CeO_2-ZrO_2 and promoted with Pd. Addition of Zn to Cu supported catalysts strongly improved WGS reaction leading to higher selectivities towards H_2 [49]. Cu-Zn/ZrO_2 and Cu-Pd/ZrO_2 based monoliths, which represented the best performance, were subjected to 15 h on-stream experiments at S/C = 3, 823 K and GHSV = 0.45×10^3 h^{-1} with undiluted reactant mixtures. Both of the monoliths maintained the H_2 selectivity of ~60-70% during the test. The initial conversions were ~50% and ~80% for Cu-Zn/ZrO_2 and Cu-Pd/ZrO_2, respectively. DME conversion over Cu-Pd/ZrO_2 started to decline rapidly after 2 h, however Cu-Zn/ZrO_2 was found to be very stable during time on stream. The authors related this observation to the presence of Cu^0-Cu^+ at the surface of the Cu-Zn/ZrO_2 accelerating formation of formate from stable methoxy species [48]. Activity of Cu-Zn/ZrO_2 turned out be strongly dependent on Cu amount in the catalyst [51]. Characterizations revealed that better dispersion of Zn particles and lower extent of sintering were the main reasons of the increase in catalytic activity at higher Zn/Cu molar ratios [51].

Yang *et al.* [52] performed DME SR experiments within a microchannel reactor coated with ZnO-Al_2O_3 catalysts. The catalyst characterizations and activity tests revealed that the performance significantly depended on the catalyst composition. The catalyst with ZnO/(ZnO + Al_2O_3) molar ratio of 0.4 was found to give the highest overall DME reforming rate, attaining complete DME conversion and H_2 space time yield of 0.31 mol g_{cat}^{-1} h^{-1} at GHSV = 7.9×10^3 h^{-1}, S/C = 2.4 and 733 K. The authors related the high catalytic activity of ZnO-Al_2O_3 to the presence of Al^{3+} and Zn^{2+} ions which was believed to be responsible for DME hydrolysis to methanol and the subsequent methanol SR, respectively. It was found that higher Al content of the catalyst could lead to a higher selectivity towards CO. Yang *et al.* [53] thereafter investigated ZnO-Cr_2O_3 coupled with TiO_2-Al_2O_3 (ZnCr-TiAl) and reported that catalytic activity was significantly enhanced over the composite catalyst. The optimal catalyst composition turned out to be ZnO-Cr_2O_3 to TiO_2-Al_2O_3 mass ratio of ~2/1. The results showed that the presence of TiO_2 could strengthen acidity and increase total acid amount due to the formation of the Al-O-Ti and Ti-O-Ti linkages. It was considered to favor DME hydrolysis leading to the excellent activity of ZnCr-TiAl in DME SR. Over 150 h long stability test, ~90% DME conversion and H_2 production rate of 0.345 mol g_{cat}^{-1} h^{-1} with no obvious deactivation were reported at 703 K, GHSV = 7.9×10^3 h^{-1} and S/C = 2.4.

Zhang *et al.* [54] prepared a γ-Al_2O_3/Al porous monolith via anodizing a commercial aluminum plate and applied Cu/γ-Al_2O_3/Al to DME SR. Anodic γ-Al_2O_3 provided higher hydrophilicity, lower apparent activation energy, and higher activity than commercial γ-Al_2O_3. Cu loading and CuO crystallite size were the two major factors affecting the catalytic activity. The best performance was observed over the catalyst with 15.9 wt% Cu and 19.2 nm CuO crystallite, giving DME 100% conversion and more than 78% H_2 yield at 598 K, S/C of 2 and GHSV of 3.6×10^3 $mL.g_{cat}^{-1}.h^{-1}$. The authors found that by applying a pre-competitive impregnation method, higher Cu dispersion and surface area could be achieved, leading to higher activity, stability and H_2 yield [55]. Byun and co-workers [56] tested anodic Al_2O_3/Al loaded with Rh for DME POX in a microchannel reactor and reported maximum H_2 yield of 86% at 723 K. They also investigated DME POX over a FeCrAl metal foam coated by a thin layer of γ-Al_2O_3 and loaded with Rh [57]. In this case, H_2 yields above 90% were obtained at temperatures up to 1023 K. In order to attain the same level of H_2 yield in the conventional packed bed reactors, much more Rh content was

reported to be employed, i.e. 5 and 10 times more Rh amount, compared to that employed in microchannel and foam structures, respectively [56, 57].

2.3. Ethylene Glycol Reforming in Intensified Catalytic Reactors

Ethylene glycol (EG) can be readily produced from acid hydrolysis of biomass and is the most abundant compound derived from the catalytic conversion of cellulose [58, 59]. EG is considered as a promising hydrogen carrier compared to other alcoholic molecules such as methanol, due to the less toxicity, inflammability and also higher theoretical energy density[58].

Izquierdoa *et al.* [60, 61] investigated SR of EG for syngas generation within microchannel reactors. The Rh/Al_2O_3 catalysts containing 1.0, 2.5 or 5.0 wt.% Rh were prepared through either conventional impregnation (Rh/Al_2O_3-ci) or separate nanoparticle synthesis (Rh/Al_2O_3-np). The catalysts fabricated using the impregnation method generally represented higher activity, especially due to the higher Rh dispersion. Under SR conditions of S/C = 4.0, GHSV = 3.0×10^5 $mL.g_{cat}^{-1}.h^{-1}$ and 948 K, complete EG converison and the maximum H_2 throughput (1.5×10^5 $mL.g_{cat}^{-1}.h^{-1}$) were attained over 2.5% Rh/Al_2O_3-ci. The selectivity towards CO and CO_2 were ~30% and ~70%, respectively. The authors also performed OSR experiments at C/O = 6.7 and 2.5% Rh/Al_2O_3-ci , again, resulted in the highest H_2 throughput. However, the same catalyst had lower selectivity towards H_2 in comparison with the catalysts supported on α-Al_2O_3 modified with CeO_2 or La_2O_3 oxides [61]. 2.5% Rh/Al_2O_3-CeO_2-ci which showed the highest surface area and pore volume, was subjected to a stability SR test. At GHSV = 2.0×10^5 $mL.g_{cat}^{-1}.h^{-1}$ and 898 K, no obvious deactivation, complete conversion and almost constant outlet concentrations of 35 mol.% and 5 mol.% were obtained for H_2 and CO, respectively, over 115 h continuous operation.

Dauenhauer *et al.* [62] prepared Rh, Pt, Rh-Ce and Rh-La based catalysts loaded on α-Al_2O_3 foams to investigate POX of EG. EG conversion was above 99% for all catalysts at GHSV $\sim10^5$ h^{-1} and C/O ratios below 1.6. The maximum H_2 selectivity was obtained at C/O ~ 1.3, where H_2 selectivity of 55, 50, 43 and 38% for Rh-La, Rh-Ce, Rh and Pt, respectively, and CO selectivity of ca. 73-77% for all the catalysts were obtained. The

authors also reported that washcoating a γ-Al_2O_3 layer onto the foam before Rh-Ce loading could significantly suppress production of minor products. ATR of EG over Rh-Ce/γ-Al_2O_3 revealed that a tunable H_2/CO ratio in the range of ~1-5 could be achieved by the addition of steam [62]. H_2 and CO selectivities of 72% and 76%, respectively, and H_2/CO of 1.7 were reported at C/O = 1.1 and S/C = 2.

Kruger *et al.* [47, 63] also performed EG ATR over Rh or Pt impregnated foams. It was reported that conversion increased from ~80% to 90% by raising C/O from 1.2 to 1.4 over Rh catalyst, while, in case of Pt catalyst, the highest conversion was around 55% at C/O = 1.2. Rh loaded foam exhibited much better performance in terms of selectivity towards syngas products, giving 45% and 73% selectivity towards H_2 and CO, respectively, over the C/O range of 1.2-1.4. EG adsorption over Rh catalyst was reported to occur via the oxygen atoms and decomposition initiated through both O-H bonds scission, followed by C-C scission yielding adsorbed formyl species which could then be decomposed to syngas products [47, 62, 63]. However, scission of only one of the O-H bonds of the adsorbed EG molecule was expected over Pt [47]. In this case, the final products were obtained through subsequent hydrogen abstractions, followed by scission of the C-C and second O-H bond [47].

2.4. Glycerol Reforming in Intensified Catalytic Reactors

Glycerol can be obtained as a byproduct through transesterification of fats and oils in biodiesel production [64]. Considering the fact that 10 m^3 glycerol is generated per every 90 m^3 biodiesel produced, developing technologies that utilize glycerol seems crucial for controlling the cost of biodiesel production [65, 66]. Due to the recent rapid demand in biodiesel, glycerol has emerged as a potential candidate for large-scale H_2 or synthesis gas production via reforming processes [3, 66]. The initiation of steam reforming of glycerol involves its decomposition into CO and H_2. The produced CO reacts with water to produce H_2 and CO_2 through WGS reaction. Glycerol is a large molecule and it is always expected that side reactions occur during its reforming, especially reactions leading to carbon deposition. Lists of this possible reversible side reaction are given as [67]:

$$C + H_2O \leftrightarrow CO + H_2 \quad (2.1)$$

$$C + 2H_2 \leftrightarrow CH_4 \quad (2.2)$$

$$CO + 3H_2 \leftrightarrow CH_4 + H_2O \quad (2.3)$$

$$CO_2 + 4H_2 \leftrightarrow CH_4 + 2H_2O \quad (2.4)$$

$$C + CO_2 \leftrightarrow 2CO \quad (2.5)$$

A feasible method to prevent coke formation is addition of oxygen to the reaction. Introducing O_2 to the system can ensure a stable reforming process with minimized catalyst deactivation during long term on-stream experiments.

Adhikari *et al.* [68] prepared various catalysts including Rh, Ni, Ru, Ir, Pd and Pt metals supported on Al_2O_3 and CeO_2/Al_2O_3 ceramic foams, and tested them in glycerol SR at 1173 K, S/C between 1 and 3 and GHSV of 1.53×10^4 h^{-1}. The results showed that Ni/Al_2O_3 and $Rh/CeO_2/Al_2O_3$ were the best performing catalysts in terms of selectivity and glycerol conversion. Conversion and H_2 selectivity increased with S/C, whereas CO selectivity remained almost constant over the whole S/C range. At S/C of 3, glycerol conversion of 90% and H_2 selectivity of 80% were reported over Ni/Al_2O_3, while $Rh/CeO_2/Al_2O_3$ resulted in 93% conversion and 71% H_2 selectivity. Both of the catalysts demonstrated ca. 80% selectivity towards CO. Increasing metal loading from 2.5% to 3.5% slightly enhanced glycerol conversion, although the selectivities remained almost the same. Adhikari *et al.* [69] also investigated another group of catalysts including Rh-Ce, Rh-Ce-Pt, Ru-Y, Ni, and Ir over ceramic foams. All the tested catalysts provided complete glycerol conversion at 973 K and GHSV of 9.2×10^4 h^{-1}, while Rh-Ce-Pt catalyst was the most selective towards H_2.

Bobadilla *et al.* [70] compared the performance of monolithic Ni-Sn based catalyst with the conventional $Ni\text{-}Sn/\gamma\text{-}Al_2O_3\text{-}MgO\text{-}CeO_2$ powder and pellet catalysts in the SR of glycerol. It was found that stability was strongly dependent on the catalyst morphology, as after only 5 h a sudden drop in H_2 yield was observed in the case of the conventional catalysts. However, all the catalysts showed the same activity and selectivity within the

first hour. Monolithic catalyst gave a stable H_2 yield of ~50% and a product distribution of 58.2% H_2, 16.1% CO and 18.1% CO_2 for 55 h. Post reaction analysis via temperature programmed oxidation analysis revealed that coke formation was minimized in the monolith, while all the active sites of the conventional catalysts were blocked by coke deposition in the pores.

Caglar *et al.* [71] conducted a modeling study to design an adiabatic microchannel reformer for H_2 production without external heat supply via SR of glycerol. SiC as the material of the reactor wall between adjacent channels was found to give higher outlet stream temperatures and glycerol conversions as compared to Al_2O_3 and SS 316. This finding was attributed to higher thermal conductivity of SiC, leading to more uniformly heated catalyst layer. Glycerol conversion and outlet temperature also increased with thickness of the wall separating the channels, as the wall was believed to be capable of operating as a medium delivering the heat from the hot inlet flow to the catalyst layer. It was estimated that an adiabatic SiC microchannel reactor consisting of 5400 channels (wall thickness = 5×10^{-4} m) and 1 kg coated Ni/CeO_2 catalyst is capable of converting ~90% of glycerol with a capacity of 4×10^3 m^3/year (inlet temperature = 873 K, S/C = 12). Park *et al.* [72] proposed a reactor configuration consisting of a Ni-foam channel for the glycerol SR and microchannels for the catalytic combustion. The numerical studies revealed an improved heat transfer between combustor and reforming channels giving a uniform temperature distribution at GHSVs above 10^5 h^{-1}.

Liu *et al.* [73] carried out ATR of glycerol over the commercial Pt and Rh/Pt dual layer monolith catalysts at GHSV of 1.5×10^4 h^{-1} and inlet temperature range of 573-973 K. They reported an increase in H_2 yield and a decrease in CO yield by changing S/C from 0.4 to 1.5, and proposed that the results might be due to the promotion of the WGS or SR reactions. It was found that at low C/O ratios (1.67-2.5) oxidation reaction was favored, which led to a reduction in the yields of H_2 and CO. C/O of 3.3, S/C of 0.8 and temperature of 973 K were found to be the optimum conditions giving 100% glycerol conversion, 75% H_2 yield, 48% CO yield and H_2/CO molar ratio of ~2 with minimal coke formation. Conducting thermodynamic equilibrium simulations, it was revealed that near-equilibrium product distribution was achieved for the selected reaction conditions [73, 74]. Liu *et al.* [75] also conducted a kinetic study on glycerol ATR. In addition to negligible mass

transfer resistance, the radial heat transfer limitation was found to be insignificant due to the approximately zero apparent heat of reaction. The kinetic expression was based on a Langmuir-Hinshelwood approach and an activation energy of 130.7 kJ mol^{-1} was determined for the reaction in which the surface reaction was reported as the rate controlling step.

The group of Schmidt [62] investigated ATR of glycerol over Rh-Ce catalyst on γ-Al_2O_3 washcoat supported on α-Al_2O_3 foam. The experiments were conducted at the catalyst backface temperature of ~1173-1473 K, C/O in the range of 0.8 to 1.6 and GHSV of ~10^5 h^{-1}. The maximum H_2 selectivity of 56% was observed at C/O = 1.2, while CO selectivity was about 80% at all C/O ratios. Steam addition at S/C = 4.5 and C/O = 0.9 lowered the temperature by ~300 K giving a maximum H_2 selectivity of 79%, CO selectivity of 25%, H_2/CO = 3.9 and less than 2% selectivity towards all minor products. H_2/CO ratio of 1.7 was obtained at C/O = 1.2, S/C = 4.5 and 1098 K resulting in H_2 and CO selectivities of 75% and 58%, respectively. H_2/CO ratios were found to be tunable also over Pt catalyst by adjusting the C/O and S/C ratios. In this case, however, a large amount non-equilibrium by-products appeared at C/O ≥ 1.4 [76].

Liu *et al.* [77] investigated the performance of $LaMnO_3$ and $LaNiO_3$-coated monoliths in the ATR of glycerol to syngas. Over $LaNiO_3$ and at a feeding rate of 0.54 mL min^{-1}, glycerol conversion decreased from 95.8% to 60.0%, while H_2 and CO selectivities increased from 50.5 to 77.6 and from 46.4 to 55.6, respectively, as the C/O ratio raised from 0.8 to 1.2. They also reported that co-feeding water at S/C = 1/3 decreased glycerol conversion by up to 10% at fuel-rich region conditions over $LaNiO_3$, but yielded about 10% higher H_2 in the tested C/O range due to the promoted SR and WGS reactions. In contrast to $LaNiO_3$, $LaMnO_3$ showed slightly better activity due to its combustion-prone nature, generating sufficient heat to sustain the autothermal operation. As a result, $LaMnO_3$ resulted mainly in CO_2 and H_2O production, while CO and H_2 were the minor products. The authors also showed that Pt loading on the $LaMnO_3$-coated monolith could significantly enhance the performance of the catalyst to deliver H_2 and CO selectivities of ~60% and ~40%, respectively at C/O = 0.8 and S/C = 1/3 [78]. Sadykov *et al.* [79, 80] studied ATR of glycerol over Ru+Ni/LaPrMnCr/YSZ, Ru+Ni/perovskite/Ni-Al and Ru+Ni/fluorite/FeCrAl microchannel plates. The obtained syngas selectivity was found to

be close to what reported by Liu *et al.* [77, 78] (~60% selectivity towards H_2 and CO). The plate microchannels, unlike perovskite-coated monoliths, could attain complete glycerol conversion. However, it is worth noting that the monoliths operated at shorter contact times (18-80 ms) than the microchannels (0.2-0.3 s) [77-80]. Sadykov *et al.* [80] also found that O_2 addition to feed in optimum amounts could suppress coking, leading to a stable performance without compromising from a decreased syngas yield.

3. EXPERIMENTAL WORK

3.1. Materials

Table 3.1 provides the source, specification and application of all the chemicals, gasses and liquids used in the experimental study.

Table 3.1. Chemicals used in catalyst preparation.

Material	Specification	Application	Source
Rhodium (III) nitrate	$Rh(NO_3)_3$ Molecular weight: 288.92	Catalyst preparation	Sigma-Aldrich
Gamma alumina (3µm)	γ-Al_2O_3 80-120 m^2/g Molecular weight: 101.96	Catalyst preparation	Alfa-Aesar
FeCrAlY	FeCrAlY sheets	Microchannel housing	Goodfellow Cambridge
Argon	99.995%	GC carrier gas	Linde
Helium	99.99%	GC carrier gas	Linde
Nitrogen	99.99%	Inert gas	Linde
Hydrogen	99.99%	Reducing agent	Linde
Oxygen	99.99%	Reactant	Linde
Glycerol	$\geq$ 99.5%	Reactant	Sigma-Aldrich
Deionized water	Conductivity: 0.1 $\mu S.cm^{-1}$	Reactant	Zeneer water purification system

3.2. Experimental Systems

Catalyst preparation system, catalyst reaction system and product analysis system are the main three experimental systems employed in this study. Catalyst preparation was conducted through an incipient-to-wetness method. The reaction system consisted of a HPLC pump to feed glycerol/water mixture to the reactor, two cold traps, three temperature controllers, and mass flow controllers, used for adjusting inlet flow rates of N_2, H_2 and O_2. Product distribution analysis was conducted with the aid of two online gas chromatographs.

3.2.1. Catalyst Preparation System

The catalyst preparation system is described schematically in Figure 3.1. Alumina supported Rh catalysts were synthesized through incipient-to-wetness method using the system shown in Figure 3.1. The system was composed of a Retsch UR1 ultrasonic mixer, silicon tubing, a vacuum pump, a Buchner flask and a Masterflex peristaltic pump employed for impregnating the support.

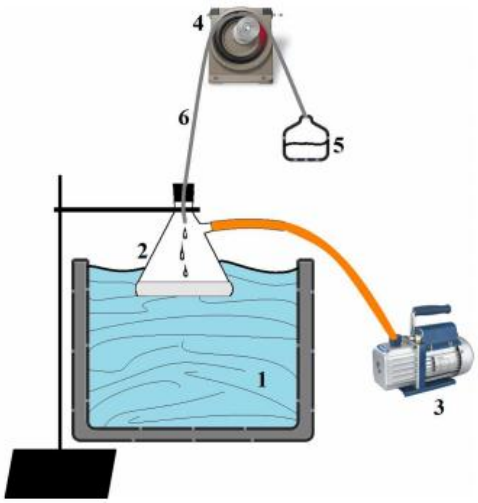

Figure 3.1. The Impregnation System: 1. Ultrasonic Mixer 2. Buchner Flask 3. Vacuum Pump 4. Peristaltic Pump 5.Aqueous Catalyst Solution 6. Silicon Tubing [81].

3.2.2. Catalytic Reaction System

The reaction system was consisted of two main sections including feed preparation section and reaction section. The feed section (Figure 3.2) was designed to introduce the liquid reactant (glycerol and deionized water mixture), inert gas (N_2), gaseous reactant (O_2) and reducing agent (H_2) to the reactor properly. A Shimadzu LC-20AD HPLC pump was utilized to feed the deionized water and glycerol mixture into the reaction system with constant and pulse-free flow. The gaseous species, N_2, O_2 and H_2, were carried through 1/8" stainless steel tubing separately from pressurized storage cylinders to the system by means of Bronkhorst F-201CV series digital mass flow controllers.



Figure 3.3. Feed Section of Glycerol Reforming System.

The process feed which is composed of the gaseous species and liquid mixture, flowing through the horizontally adjusted 1/16” stainless steel tube, was directly sprayed into the 2.0 cm ID x 80 cm quartz reactor located in the furnace (Figure 3.3). The reactant mixture was fed to the reactor without pre-heating through a 1/16" injector pipe. In order to introduce liquid reactant mixture into the reactor effectively, different length of injectors were examined and it was found that the one which went as far as 10 cm into the first zone of furnace resulted in the most accurate and stable process.



Figure 3.3. Furnace and Reaction Section of Glycerol Reforming System.

A PROTHERM PZF 12/50/500 furnace, composed of three zones and three temperature controllers, was utilized to adjust the reaction temperature. In order to guarantee vaporization of liquid mixture, the temperature of the first zone was kept between 310-350 °C. The microchannel was placed in the second zone where the temperature was set as the reaction temperature. The temperature of the following zone

was set at 310 °C to prevent condensation on the walls of quartz tube. The product stream leaving the reactor was directed through two cold traps before it reached the gas chromatographs for analysis (Figure 3.4). The main purpose of the cold traps was to ensure the complete removal of condensables (glycerol, water or any heavy product), preventing tubes blockage and gas chromatographs damage. Between the first and the second cold trap, a three way valve was placed in order to provide the opportunity either to trap N_2 in the quartz tube, to send the gas to soap bubble meter to monitor gas flows or to send the product stream to the gas chromatographs.



Figure 3.4. Post-reaction Section of Glycerol Reforming System.

3.2.3. Product Analysis System

The product stream was composed of inert nitrogen, hydrogen, carbon monoxide, methane, carbon dioxide, ethylene and ethane, on dry basis. Nitrogen, hydrogen, carbon monoxide and methane were detected by Shimadzu GC-2014 gas chromatograph, equipped with a Molecular Sieve 5A column and a thermal conductivity detector (TCD). Carbon dioxide, ethylene and ethane were quantified by Shimadzu GC-8A gas

chromatograph, equipped with a Porapak Q column and a TCD. The stream coming from the cold trap is sent continuously to Shimadzu GC-8A and after gas sampling, the flow is diverted to Shimadzu GC-2014. Calibration of both gas chromatographs was carried out by injecting the known volumes of each species through the injection ports through the columns under conditions given in Table 3.2. The area under each of the peaks, representing a specific product in the stream, were calculated and then plotted against the known volumes to construct the calibration curves given in Appendix A.

Sampling in both units is carried out by six-way valves that are set to inject 1 mL of gas sample via sample loops to each chromatograph. During the experiments, the first datum is recorded after 30 minutes, and then each datum is taken in every 45 minutes. The results were reported based on the arithmetic average of the data after the system reaches a steady state after ~120 minutes.



Figure 3.5. Gas Chromatographs Used in Glycerol Reforming System.

Table 3.2. GC conditions for product gas analysis.

GC Parameter	Shimadzu GC-2014	Shimadzu GC-8A
Detector type	Thermal conductivity	Thermal conductivity
Column oven temperature	50 °C	90 °C
Injector temperature	80 °C	90 °C
Detector temperature	150 °C	150 °C
Carrier gas	Argon	Helium
Carrier gas flow rate	25 $mL.min^{-1}$	25 $mL.min^{-1}$
Detector current	50 µA	120 µA
Column packing material	Molecular Sieve 5A (60-80 mesh)	Porapak Q (80-100 mesh)
Column tubing material	Stainless steel	Stainless steel
Column ID & length	1/8" OD x 2 m	1/8" OD x 3 m
Sampling loop	1 mL	1 mL

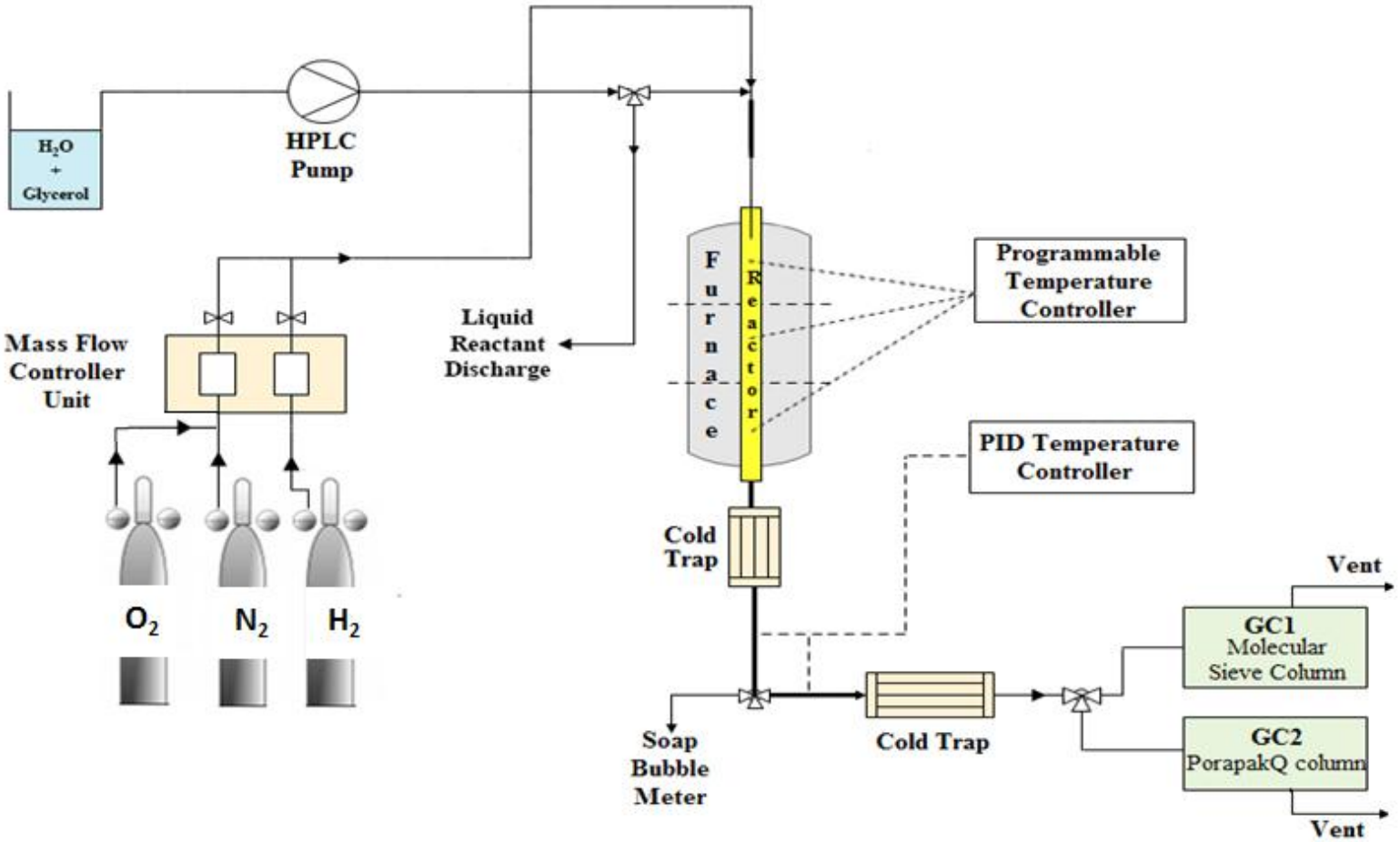

Figure 3.6. Schematic Diagram of the Reaction System.

3.3. Catalyst Preparation and Pretreatment

Rh/Al_2O_3 catalysts were synthesized by incipient to wetness impregnation method. The following sections explain catalyst preparation steps which consisted of support preparation, active catalyst preparation, microchannel coating and catalyst pretreatment.

3.3.1. Preparation of Support

Glycerol reforming usually requires high temperatures; therefore, stable catalyst is a crucial issue that is needed to be tackled to enable a stable process. In this study, alumina was used as the support and rhodium as the catalyst active phase. Low stability of γ-Al_2O_3 which provides the highest surface area and low surface area of α-Al_2O_3 which is the most stable alumina phase made δ-phase of alumina the best possible option to be utilized as a support for the active metal. Therefore, based on a study conducted by Avci *et al.* [82], in order to obtain a support with high surface area and thermal stability, 3-μm sized γ-Al_2O_3 were dried at 150 °C for 2 hours and calcined at 900 °C for 4 hours. Avci *et al.* [82] reported BET surface area of 81.6 $m^2\ g^{-1}$ for the obtained δ-Al_2O_3 support**.**

3.3.2. Preparation of Active Catalysts

2 wt.% Rh/Al_2O_3 was prepared in 2 g batches using incipient-to-wetness impregnation method. The amounts of Rh and Rh-containing precursor ($Rh(NO_3)_3$, Sigma-Aldrich) were calculated and the solution containing Rh precursor was put into a beaker. Deionized water was added into the beaker, until the total amount in the beaker was 4.0 mL (~1.7 $mL_{solution}\ g^{-1}{}_{support}$). The solution of metal precursor was carefully impregnated over the support to obtain homogeneous slurry mud of catalyst using a peristaltic pump under vacuum condition (Figure 3.1). The resulting slurry was mixed ultrasonically for 90 minutes under vacuum and dried at 120 °C for 16 hours. The obtained powder was crushed to obtain fine particles, and then was calcined at 600 °C for 3 hours.

3.3.3. Catalyst Coating on Microchannel Plates and Pretreatment

FeCrAlY plates (Goodfellow) were obtained having the dimensions 2 mm × 5 mm × 20 mm, cleaned and then calcined in furnace at 900 °C for 2 hours to enhance the adhesion of the coated plates by forming a native alumina layer on the plates. The plates were rasped on their edges, coated and fit into the cylindrical housing (Figure 3.7) to give a catalytic microchannel with of dimensions of 7.5×10^{-4} m (H) × 4×10^{-3} m (W) × 2×10^{-2} m (L). The 310-grade stainless steel cylindrical housing with a diameter of 18.6 mm and a length of 30 mm was manufactured by wire electrodischarge machining technique.

The plates were blade coated to reach ~0.02 grams of catalyst per cm^2 of plate surface. For this purpose, a slurry with water-to-powder ratio of 5:1 was coated over the plate to reach 0.035-0.040 grams of slurry per cm^2 of plate surface. The coated plates were dried at 120 °C for 16 hours and calcined at 600 °C for 3 hours. After inserting the plate into the housing, a piece of quartz wool was stuck into the bottom of the housing to ensure the plate was kept still during the reaction. Before starting the experiment, the active phase of the catalyst had to be reduced from oxidized states to metallic states. Therefore, 40 NmL min^{-1} H_2 flow was passed over the catalyst at 800 °C for 2 hours.

3.4. Reaction Tests

Glycerol OSR experiments are conducted in a quartz tube in which the housing and the 2% Rh/Al2O3 catalyst coated plate are placed (Figure 3.7). Two pieces of quartz wool are also utilized to keep the coated plate immobilized in the housing and to enable visually detection of possible coke formation during the reforming process. The housing and quartz tube are designed such that the annulus-shaped gap between the hosing and tube is blocked after expansion of the housing at reaction temperatures, preventing any bypass flow. The tube is placed inside the furnace with three zones each of which controlled by a PID controller. The temperature of the middle zone is the reaction temperature under which the reforming process takes place. Glycerol oxidative steam reforming experiments are conducted to investigate the effects of temperature (550-700 °C), steam-to-carbon ratio (S/C = 3-5) and carbon-to-oxygen ratio (C/O = 0.75-2.25) at total flow of 96 NmL min^{-1}.

S/C and C/O default values are 5 and 1.125, respectively, and are subjected to change only at time of studying their individual effects.

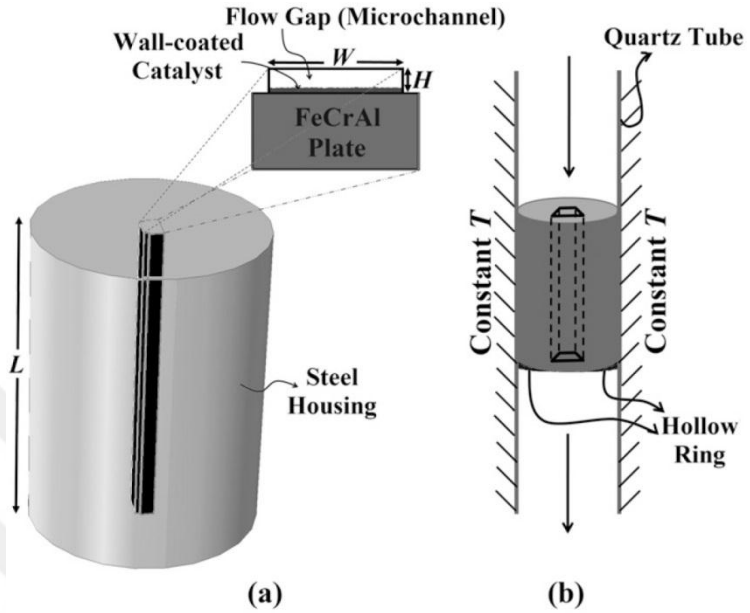

Figure 3.7. Microreactor Configuration a. Coated Microchannel Reactor b. Location of Steel Housing in Quartz Tube [81].

4. MODELING AND SIMULATION

Steam reforming of glycerol in a heat exchange integrated microchannel reactor involving solid wall separated, parallel reaction and heating channels is investigated by means of a mathematical model-based parametric study, and the impact of operational and structural parameters on heat distribution and on glycerol conversion are explored. Detailed description of the microchannel reactor and the mathematical model are given in in this chapter.

4.1. Description of the Microchannel Reactor, Model Equations and Assumptions

The heat-exchange integrated microchannel reactor concept, in which parallel groups of heating and reaction (reforming) channels are separated by the solid reactor wall is presented in Figure 4.1. Inner walls of the reaction channels, each of which having dimensions of 6.5×10^{-4} m height, 1×10^{-2} m width and 5×10^{-2} m length, are uniformly coated with 5×10^{-5} m thick layers of porous Co-Ni/Al_2O_3 catalyst. The heating channels, having the same dimensions with the reforming channels, carry the hot fluid (steam) flowing in the opposite direction of the reactive stream, whose inlet is composed of $C_3H_8O_3$ vapor, steam and nitrogen (Figure 4.1). It is assumed inlet flow fed to every channel is uniform in terms of flow rate and composition. Particular positioning of the channels indicate that (i) the same phenomenon, i.e. either heating or reaction is taking place in the same horizontal group of channels, and (ii) lateral heat flow (occurring in *x*-direction) between two channels of the same group counter-balance each other. Therefore, heat transfer within the same group of channels (i.e. in the *x*-direction) is assumed to be negligible, and only the heat flow in the *y*-direction is taken into account, and the behavior of the multichannel unit is represented by the unit cell, the representative and repeating unit of the complete reactor (Figure 4.1). Moreover, as the height of the channel is much smaller than its width to give an aspect ratio (height/width) of 0.065, axial dispersion can be neglected and uniform diffusion mixing can be assumed [83]. It is also worth noting that exterior surfaces of the multichannel reactor are considered to be ideally insulated, and any heat exchange with the surroundings is neglected. Based on the implications stated above,

simultaneous reaction, fluid flow and heat transfer within the unit cell can modeled by the Navier-Stokes equations describing the steady state conservation of mass, momentum and energy in two-dimensional (2D) Cartesian coordinates as given in their generalized forms in Table 4.1. Validity of representing a heat-exchange integrated multichannel reactor with a 2D unit cell is presented in the literature in which the difference between the temperature distribution predictions of three-dimensional (3D) modeling of a microreactor block (similar to that shown in Figure 4.1) and 2D modeling of a unit cell is found to be less than only ~5 K [84].

Table 4.1. Model equations in 2D cartesian coordinates.

Continuity equation	$\nabla \cdot \left(\rho_m \vec{\mathbf{v}}\right) = 0$
Momentum conservation (fluid phases in reforming and heating channels)	$\nabla \cdot \left(\rho_m \vec{\mathbf{v}}\vec{\mathbf{v}}\right) = -\nabla p + \nabla \cdot \left[\mu_m \left(\nabla \vec{\mathbf{v}} + \left(\nabla \vec{\mathbf{v}}\right)^{\mathrm{T}} - \frac{2}{3}\left(\nabla \cdot \vec{\mathbf{v}}\right)\mathbf{I}\right)\right]$
Momentum conservation (catalytic washcoat phase in reforming channel)	$\nabla \cdot \left(\rho_m \vec{\mathbf{v}}\vec{\mathbf{v}}\right) = \vec{\mathbf{F}} - \nabla p + \nabla \cdot \left[\mu_m \left(\nabla \vec{\mathbf{v}} + \left(\nabla \vec{\mathbf{v}}\right)^{\mathrm{T}} - \frac{2}{3}\left(\nabla \cdot \vec{\mathbf{v}}\right)\mathbf{I}\right)\right]$ $\vec{\mathbf{F}} = -\left(\frac{\mu_m}{\alpha}\vec{\mathbf{v}} + \frac{C_2}{2}\rho_m \left\|\vec{\mathbf{v}}\right\| \vec{\mathbf{v}}\right),$ $\alpha = \frac{d_p^2}{150}\frac{\varepsilon_{cat}^3}{\left(1-\varepsilon_{cat}\right)^2},\ C_2 = \frac{3.5}{d_p}\frac{\left(1-\varepsilon_{cat}\right)}{\varepsilon_{cat}^3}$
Species mass conservation (fluid phases in reforming and heating channels)	$\nabla \cdot \left(\rho_m \vec{\mathbf{v}} Y_i\right) = -\nabla \cdot \vec{J}_i$ $\vec{J}_i = -\rho_m D_{i,m} \nabla Y_i$
Species mass conservation (catalytic washcoat phase in reforming channel)	$\nabla \cdot \left(\rho_m \vec{\mathbf{v}} Y_i\right) = -\nabla \cdot \vec{J}_i + M_i R_i \rho_{cat}$ $\vec{J}_i = -\rho_m D_{eff,i,m} \nabla Y_i$
Energy equation conservation (fluid phases in reforming and heating channels)	$\nabla \cdot \left(\rho_m c_{p,m} \vec{\mathbf{v}} T\right) = \nabla \cdot \left(k_m \nabla T\right)$
Energy equation (catalytic washcoat phase in reforming channel)	$\nabla \cdot \left(\rho_m c_{p,m} \vec{\mathbf{v}} T\right) = \nabla \cdot \left(k_{eff,m} \nabla T\right) + \sum_{rxn} \left(-\Delta H_{rxn}\right)\left(r_{rxn}\right)\rho_{cat}$ *rxn*=DEC (Reaction 2), WGS (Reaction 3), MET (Reaction 6)
Energy equation (solid wall between the channels)	$\nabla \cdot \left(k_w \nabla T\right) = 0$

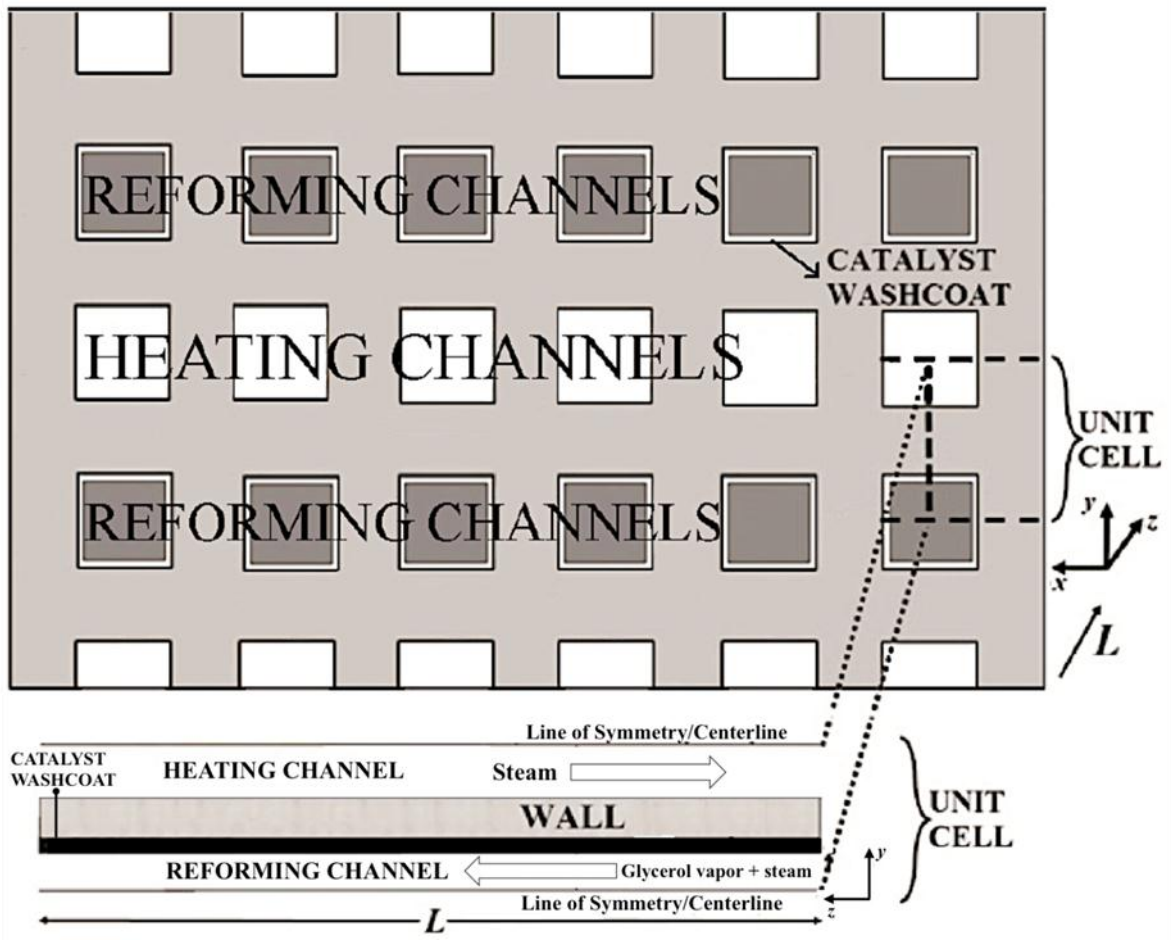

Figure 4.1. Heat-exchange integrated microchannel reactor and the unit cell (channel dimensions are not to scale).

Model equations given in Table 4.1 consider the existence of three phases, namely the fluid phase, catalytic washcoat phase and the solid wall phase in the unit cell. The fluids, mixture of glycerol vapor, steam and nitrogen in the reaction channel and steam in the heating channel, are assumed to be of Newtonian type. Gravitational effects are neglected, and, therefore, not considered in the momentum conservation equations. Since the simulations are carried out at atmospheric pressure and the pressure drop is reported to remain below ca. 2% [85, 86], the fluids are considered as ideal and incompressible. Reynolds number is equal to ~40 so the flow regime in the reactor is laminar. The solid wall between the channels is impermeable to material flow, but affects heat transfer within the reactor via thermal conduction in *y*- and *z*-directions as modeled in Table 4.1.

Table 4.2. Correlations used to predict physical properties of the reactive mixture and porous catalyst layer.

Physical property	**Correlation**	**Ref.**
Viscosity of the reactive mixture	$\mu_m = \sum_{i=1}^{N_g} \frac{y_i \mu_i}{\sum_{j=1}^{N_g} y_j \Phi_{ij}}$ $\Phi_{ij} = \frac{1}{\sqrt{8}} \left(1 + \frac{M_i}{M_j}\right)^{-1/2} \left[1 + \left(\frac{\mu_i}{\mu_j}\right)^{1/2} \left(\frac{M_j}{M_i}\right)^{1/4}\right]^2$	[87]
Thermal conductivity of the reactive mixture	$k_m = \sum_{i=1}^{N_g} \frac{y_i k_i}{\sum_{j=1}^{N_g} y_j \Phi_{ij}}$	[88]
Effective thermal conductivity of the reactive mixture within the catalyst layer	$k_{eff,m} = \varepsilon_{cat} k_m + (1 - \varepsilon_{cat}) k_{cat}$	[88]
Diffusivity of species *i* in the reactive mixture	$D_{i,m} = \frac{1 - y_i}{\sum_{j=1}^{N_g} y_i / D_{ij}}, \qquad j \neq i$	[88]
Binary diffusivity	$D_{ij} = \frac{10^{-3} T^{1.75} \left(\frac{1}{M_i} + \frac{1}{M_j}\right)^{1/2}}{p\left[\left(\sum \upsilon\right)_i^{1/3} + \left(\sum \upsilon\right)_j^{1/3}\right]^2}$	[89]
Effective diffusivity of species *i* in the catalyst layer	$D_{eff,i,m} = \frac{\varepsilon_{cat}}{\tau_{cat}} \left[\frac{1}{D_{K,i}} + \frac{1}{D_{i,m}}\right]^{-1}$	[90]
Knudsen diffusivity for species *i*	$D_{K,i} = 48.5 d_{pore} \sqrt{\frac{T}{M_i}}$	[90]
Pore diameter of the catalyst layer	$d_{pore} = \frac{4 V_{pore}}{S_{BET}}$	[91]
Heat capacity of the reactive mixture	$c_{p,m} = \sum_{i=1}^{N_g} c_{p,i} Y_i$	–
Density and molecular weight of the reactive mixture	$\rho_m = \frac{p M_m}{RT}, \quad M_m = \sum_{i=1}^{N_g} M_i y_i$	–

Correlations used to evaluate viscosity, diffusivity, heat capacity and thermal conductivity of the reactive mixture together with the correlations for effective diffusivity and thermal conductivity within the catalyst layer are presented in Table 4.2 [87-91]. The correlations were applied to estimate the physical properties of the fluids at the respective feed temperature, and the needed input data for the correlations were extracted from [92] and [93]. In order to reduce the computation time, temperature dependency of the physical properties is neglected. The validity of this assumption is demonstrated elsewhere [94]. Porosity, tortuosity, BET surface area and thermal conductivity of the catalyst layer, which is assumed as a homogeneous porous medium, are taken as 0.54, 1.7, 166 $m^2.g_{cat}^{-1}$ and 13.0 $W.m^{-1}.K^{-1}$, respectively [5, 92, 95]. While calculating the permeability and inertial resistance coefficient of the washcoat existing in momentum conservation equation of the catalyst layer (Table 4.1), particle diameter (d_p) is taken equal to the washcoat thickness of 5×10^{-5} m. Pores of the catalyst layer, with the volume of 0.57 $cm^3.g_{cat}^{-1}$ [5] are assumed to be cylindrical with pore diameter equal to 1.37×10^{-8} m as calculated by the equation provided in Table 4.2.

4.2. Kinetic Model

In addition to glycerol decomposition (Reaction 1.2) and WGS (Reaction 1.3) that combine to give the primary route of SR via Reaction 1.1, several side reactions are reported to affect product distribution. Owing to the fact that methane is an important side product of glycerol SR [5], the reaction network is assumed to be composed of Reactions 1.2 and 1.3, together with the methanation (MET) given below:

$$CO + 3H_2 \rightarrow CH_4 + H_2O,\ \Delta H° = -206\ kJ\ mol^{-1} \qquad (4.1)$$

The model reactions 1.2, 1.3 and 4.1 are driven by a layer of Co-Ni/Al_2O_3 catalyst, the porous washcoat phase, in which the fluid flow is modeled by the equations provided in Table 4.1. Since the initiation times needed for homogeneous reactions are longer than that required for the heterogeneous ones under the pertinent operating conditions, gas-phase reactions are neglected [96]. Glycerol SR over Co-Ni/Al_2O_3 catalyst is described by Cheng

et al. [5] proposing power law type kinetics (Equation 4.2) with estimated parameters for the total rate of generation/consumption of the species *i* (R_i):

$$R_i = (\upsilon_i) A e^{-E_A/RT} p_{\text{glycerol}}^{\beta} p_{\text{H}_2\text{O}}^{\gamma} A_{\text{metal}} \tag{4.2}$$

where υ of +1 and -1 stand for production and consumption of species *i* and A_{metal} is equal to 740 $m^2.kg_{cat}^{-1}$ [5]. According to the reaction scheme, glycerol consumption, and CO_2 and CH_4 production rates stand for the rates of DEC, WGS and MET, i.e. Reactions 1.2, 1.3 and 4.1, respectively [5]:

$$r_{\text{DEC}} = -R_{\text{glycerol}} \tag{4.3}$$

$$r_{\text{WGS}} = R_{\text{CO}_2} \tag{4.4}$$

$$r_{\text{MET}} = R_{\text{CH}_4} \tag{4.4}$$

Therefore the rates of production/consumption of CO, H_2 and H_2O can then be expressed as follows:

$$R_{\text{CO}} = 3r_{\text{DEC}} - r_{\text{WGS}} - r_{\text{MET}} \tag{4.5}$$

$$R_{\text{H}_2} = 4r_{\text{DEC}} + r_{\text{WGS}} - 3r_{\text{MET}} \tag{4.6}$$

$$R_{\text{H}_2\text{O}} = -r_{\text{WGS}} + r_{\text{MET}} \tag{4.7}$$

Values of the parameters of Equation 4.2 estimated by Cheng *et al.* [5] are presented in Table 4.3.

Table 4.3. Kinetic parameters for the glycerol, CO_2 and CH_4 consumption/generation [6].

Species	***A*** **(mol.m^{-2}.s^{-1}.kPa$^{-(\beta+\gamma)}$)**	***E_A*** **(kJ.mol^{-1})**	***β***	***γ***
$C_3H_8O_3$	0.036	63.30	0.253	0.358
CO_2	0.074	64.06	0.281	0.403
CH_4	0.555	100.90	0.601	0.393

4.3. Numerical Solution

The 2D model equations are solved numerically by the finite volume method on ANSYS 16.0 platform. Solution domain, i.e. the unit cell presented in Figure 4.1 is discretized by 16600 rectangular and triangular cells in the reforming channel, 9600 triangular cells in the wall zone and 4000 cells in the heating channel. Such a discretization scheme is found to deliver mesh independent solutions, which remained almost unaffected in case of finer meshing with higher number of cells. The kinetic expressions (Equations 4.5–4.7) together with the correlations provided in Table 4.2 are introduced in the form of user-defined functions. Boundary conditions at the entrance of each channel are implemented as the respective inlet values of velocity, species mass fraction and temperature. Exit pressure is specified as the outlet boundary conditions for each channel. Conditions associated with the catalyst layer-gas interface involve continuity of velocity, and fluxes of heat and species mass. Fluxes of quantities across the symmetry lines as well as component of velocity normal to the symmetry line are taken as zero. The remaining boundaries in the model are considered as no-slip, impermeable walls where species mass and heat fluxes do not exist. Numerical execution of the model equations are carried out on an HP Z620 workstation involving 2 × 2.00 GHz Xeon^{TM} processors and 32 GB of memory. Duration of the each simulation lasted between 15-20 h, depending on the particular combination of operating conditions.

The mathematical model described above is used to carry out a parametric study for providing insight into the response of glycerol SR driven in a microchannel reactor with an integrated heat exchange function. For this purpose, the effects of operational parameters, namely velocity and temperature of hot fluid (steam) at the inlet, flow direction of the steam, feed temperature and composition (S/C) of the reactive mixture, and structural parameters, i.e. reactor wall material and thickness of the wall between the reforming and heating channels on temperature distribution and glycerol conversion are investigated. During the simulations, the investigated parameter is changed according to its values/attributes presented in Table 4.4, while the other parameters are kept at their default values/attributes. In its default configuration the microchannel reactor is made of AISI steel (4340 type) and involves 6×10^{-4} m thick walls between the channels. Default reactor operation involves counter-current flow of reactive mixture, fed at 723 K, and steam fed at

a temperature and inlet flow rate of 723 K and 5 m/s, respectively. Molar flow rates of steam, glycerol vapor and nitrogen at the inlet of the reaction channel are taken as 1.50×10^{-4} mol/s, 1.25×10^{-5} mol/s and 7.75×10^{-5} mol/s, respectively. The corresponding S/C ratio of 4 ensures coke-free operation over the catalyst in the range of conditions investigated in this study [97]. Operating conditions are selected in a way that they are in alignment with the ones run in the kinetic model. During investigation of the effect of S/C, molar flow rate of glycerol is kept constant, while steam flow rate is changed accordingly to obtain the desired ratio. Molar flow rate of nitrogen is adjusted accordingly to keep the total inlet molar flow rate constant at 2.40×10^{-4} mol/s.

Table 4.4. Investigated parameters and their respective range/attributes.

Parameter	**Investigated values/range**
S/C	1-6
Direction of reactive flow and steam	Counter-current, Co-current, Without steam
Inlet temperature of steam (K)	663-783
Inlet temperature of the reactive mixture (K)	673-773
Inlet velocity of steam ($m.s^{-1}$)	2-8
Thickness of the wall between the channels (m)	4×10^{-4}-1.2×10^{-3}
Reactor material	Cordierite, AISI Steel, Silicon Carbide (SiC)

5. RESULTS AND DISCUSSION

5.1. Oxidative Steam Reforming of Glycerol in a Catalytic Microchannel

This section includes the outcomes of the experimental investigation of microchannel enabled steam reforming of glycerol. The effects of reaction temperature, S/C and C/O ratios on glycerol conversion (Equation 5.1) and product yields (Equation 5.2) are presented in following sections.

$$X_{glycerol} = 100 \times \frac{\text{moles of carbon in gaseous products}}{3 \times \text{moles of glycerol in the feed}} \quad (5.1)$$

$$Yield_i = \frac{\text{moles of species "i" in gaseous products}}{\text{moles of glycerol feed}} \quad (5.2)$$

The dry basis conversion is calculated via detected carbon containing species in the gaseous product stream. CO, CO_2, CH_4, C_2H_4 and C_2H_6 are the carbon containing species detected through GC analysis. Thermodynamic analysis calculations predicts that generation of other hydrocarbons are highly suppressed under the reforming conditions as Koc and Avci [98] reported total molar composition of less than 1%. Additionally, it is assumed that no carbon containing liquid is produced via the process. The conversion formula also does not take coke formation into account. Product yields of H_2, CH_4, CO, CO_2 and C_{1+} (sum of C_2H_4 and C_2H_6 yields) were calculated based on Equation 5.2 by dividing moles of the product in the outlet to the moles of glycerol fed in the inlet.

5.1.1. Effect of Temperature on Glycerol Oxidative Steam Reforming

Effect of temperature on glycerol conversion and product yields was examined at S/C of 5 and C/O of 1.125 over 550-700 °C range (Figure 5.1). The blank test (Table 5.1) shows that glycerol conversion is occurring homogeneously and the presence of catalyst affects the product distribution significantly providing a much higher H_2 and CO_2 yields.

Increasing temperature from 550 °C to 600 °C resulted in glycerol conversion elevation from 93% to 100%. This is attributed to the endothermic nature of glycerol decomposition which is favored at higher temperatures. Complete glycerol conversion was observed over the temperature range of 600-700 °C. By raising temperature from 550 °C to 600 °C, glycerol conversion increased from 93.4% to 100%, resulting in a slight increase in H_2 yield. The increase in H_2 yield between 550 °C and 600 °C can be attributed to the accelerated glycerol decomposition (Reaction 1.2) rate to H_2 and CO. However, H_2 could be also consumed in methanation (Reaction 4.1) which hindered further H_2 production and resulted in a higher CH_4 yield (Table 5.1).

Table 5.1. Product yields over 550-700 °C range at C/O 1.125 and S/C of 5.

Temperature (°C)	**Conversion (%)**	**Product Yields (mol/mol glycerol fed)(×10)**				
		H_2	**CH_4**	**CO**	**CO_2**	**C_{1+}**
550	93.4	13.7	1.3	16.5	8.2	1.0
600	100	14.3	1.9	18.7	7.9	1.2
650	100	18.9	1.8	16.8	10.5	1.2
700	100	23.0	1.7	15.1	12.3	0.9
700 (blank test)	100	14.1	2.2	20.9	7.0	1.3

On the other hand, by raising temperature from 600 °C to 650 °C and from 650 °C to 700 °C, it is clearly observed that H_2 elevation gets much more pronounced. This suggests that glycerol reforming to H_2 is highly favored at temperatures above 600 °C. The elevation of CO_2 generation with temperature can be attributed to accelerated glycerol POX (Reaction 1.4) at higher temperatures, which consequently reduces CO yield. The opposing response of CO and CO_2 yields can be also explained by WGS reaction. Raising temperature would also improve in-situ coke gasification:

$$C\ (s) + H_2O \rightarrow CO + H_2,\ \Delta H° = 131\ kJ.mol^{-1} \qquad (5.3)$$

Therefore, the generated CO might shift WGS reaction towards further CO_2 and H_2 production. Figure 5.2 shows H_2/CO can be adjusted by temperature to achieve a desired ratio. Lower CO generation also impedes methanation reaction, and consequently, CH_4 yield is decreased at temperatures above 600 °C. This also holds for C_{1+} yields possibly due to domination of glycerol oxidation which suppresses the side reactions.

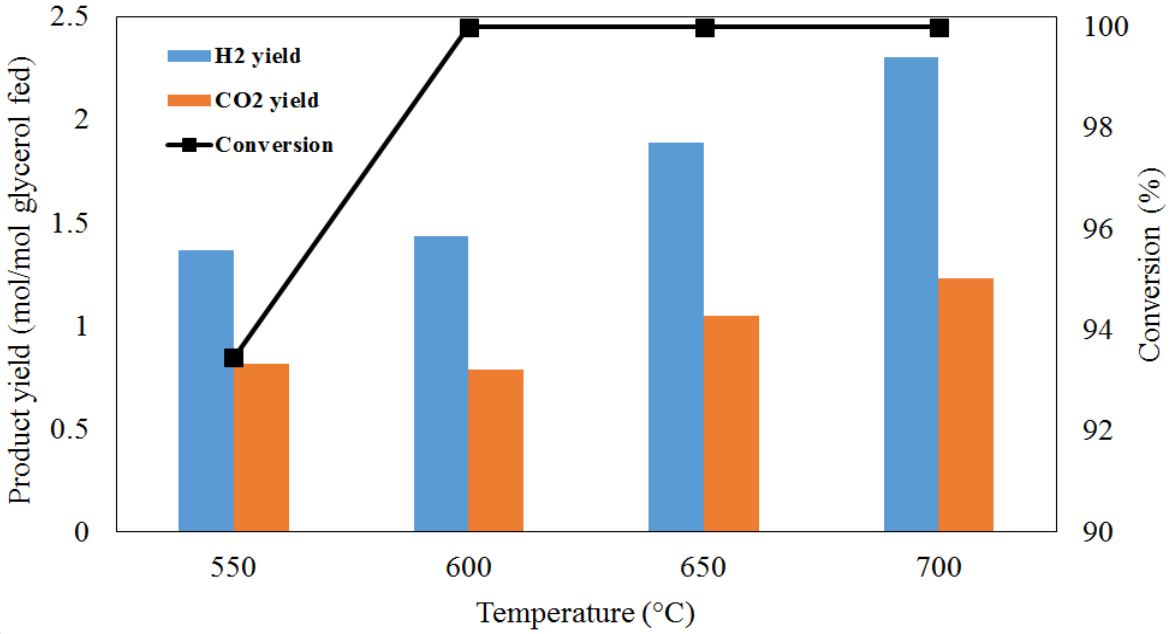

Figure 5.1. Temperature effect on glycerol OSR.

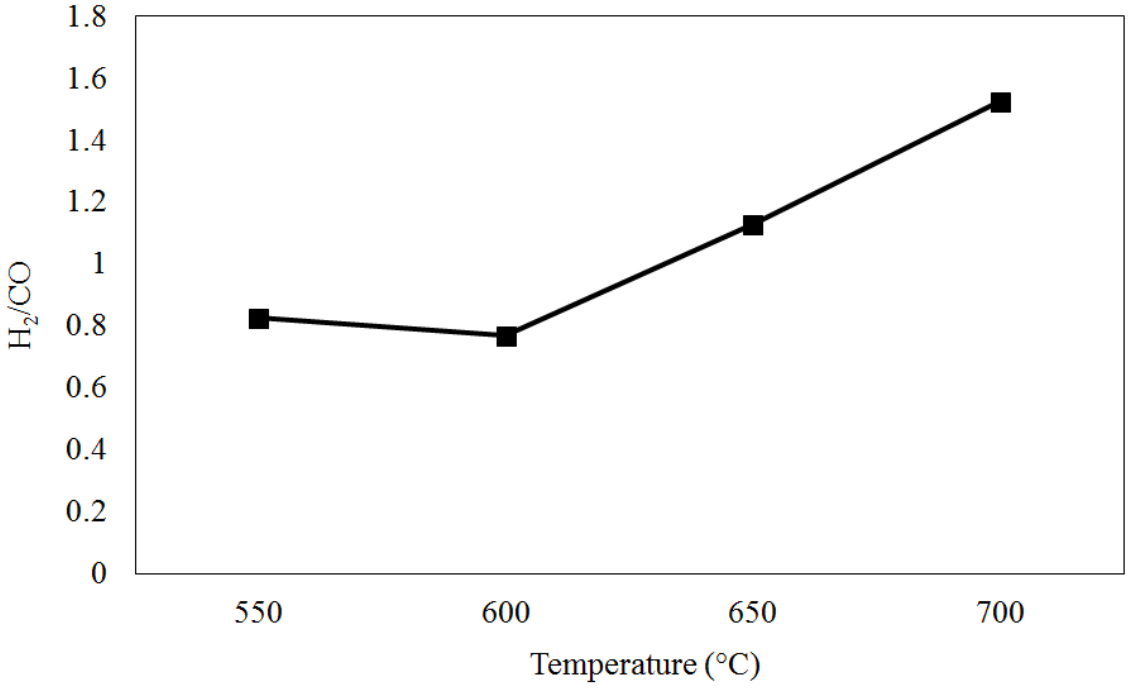

Figure 5.2. Effect of temperature on outlet H_2/CO ratio.

5.1.2. Effect of C/O on Glycerol Oxidative Steam Reforming

At temperatures of 550 °C and 700 °C, the effect of C/O in the feed on the glycerol oxidative steam reforming and product yields is studied (Table 5.2 and Figures 5.3-5.4). Glycerol conversion increases with O_2 content of the feed from 82.0% to 100%; however, over the studied C/O range of 0.75-2.25 complete glycerol conversion is observed at 700 °C. It is found that H_2 yield is enhanced with C/O as the lower amount of O_2 in the feed could allow glycerol to be reserved for conversion thorough routs in which H_2 generation is favored rather than consuming it in total oxidation. Accordingly, it is clearly observed that with decreasing C/O, CO_2 production is increased as glycerol total oxidation is favored.

Table 5.2. Product yields over C/O range of 0.75-2.25 at S/C of 5 and two temperatures (550 °C and 700 °C).

Temperature (°C)	**C/O**	**Conversion (%)**	**Product Yields (mol/mol glycerol fed)(×10)**				
			H_2	**CH_4**	**CO**	**CO_2**	**C_{1+}**
550	0.75	100	10.8	0.8	21.1	11.0	0.4
	1.125	93.4	13.7	1.3	16.5	8.2	1.0
	2.25	82.0	21.5	1.3	12.2	8.5	1.3
700	0.75	100	16.5	0.5	14.4	16.6	0.3
	1.125	100	23.0	1.7	15.1	12.3	0.9
	2.25	100	26.7	3.1	18.5	9.4	3.6

Effect of C/O ratio on H_2 yield is found to be more significant at 550 °C. This can be due to the fact that WGS reaction is suppressed high temperatures. On the other hand, CO_2 yield is more responsive to C/O ratio at 700 °C which suggests that glycerol conversion was favored through oxidation at this temperature. This can be also confirmed by the opposing trends of CO yield at 550 °C and 700 °C. At lower temperature where WGS might play a more significant role, CO yield decreased with C/O, however, at 700 °C where oxidation can be the dominant reaction, CO yield increased due to the lack of O_2, hindering oxidation. The dramatic decrease of CH_4 and C_{1+} yields at 700 °C can be also explained by oxidation domination and WGS suppression and high temperatures. Another possible reason for the increase in CO yield and rather dramatic decrease in CO_2 yield with

C/O at 700 °C can be Boudouard reaction ($C+CO_2 \rightarrow 2CO$) which is an endothermic reaction favored at higher temperatures.

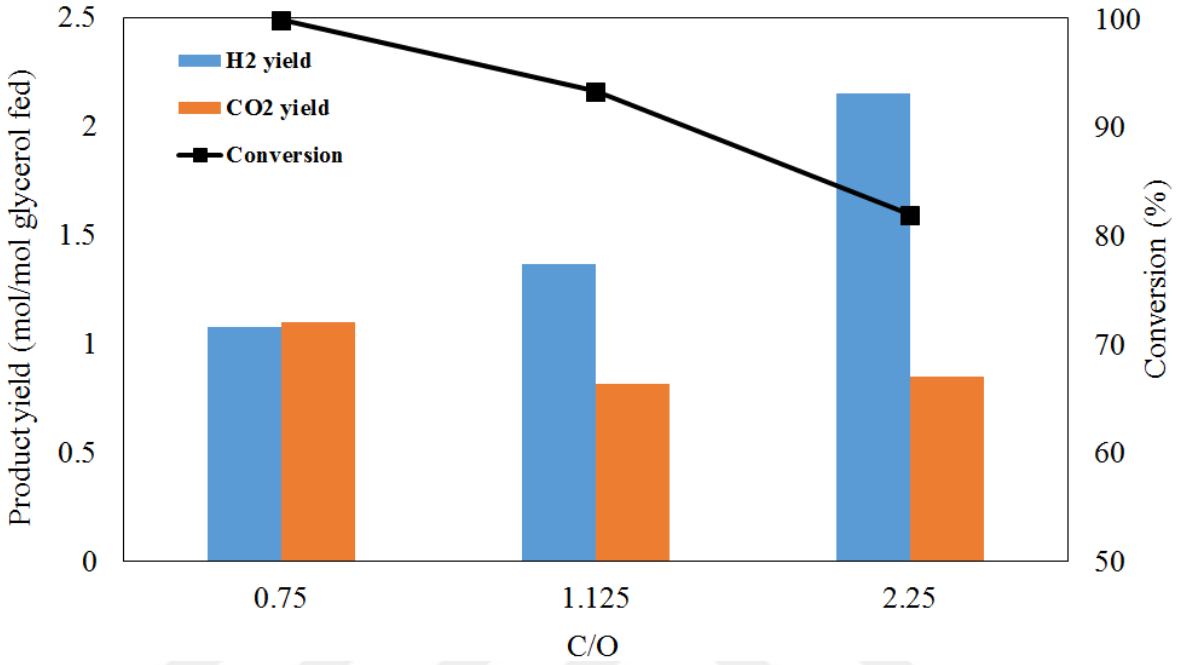

Figure 5.3. Effect of C/O on glycerol OSR at 550 °C.

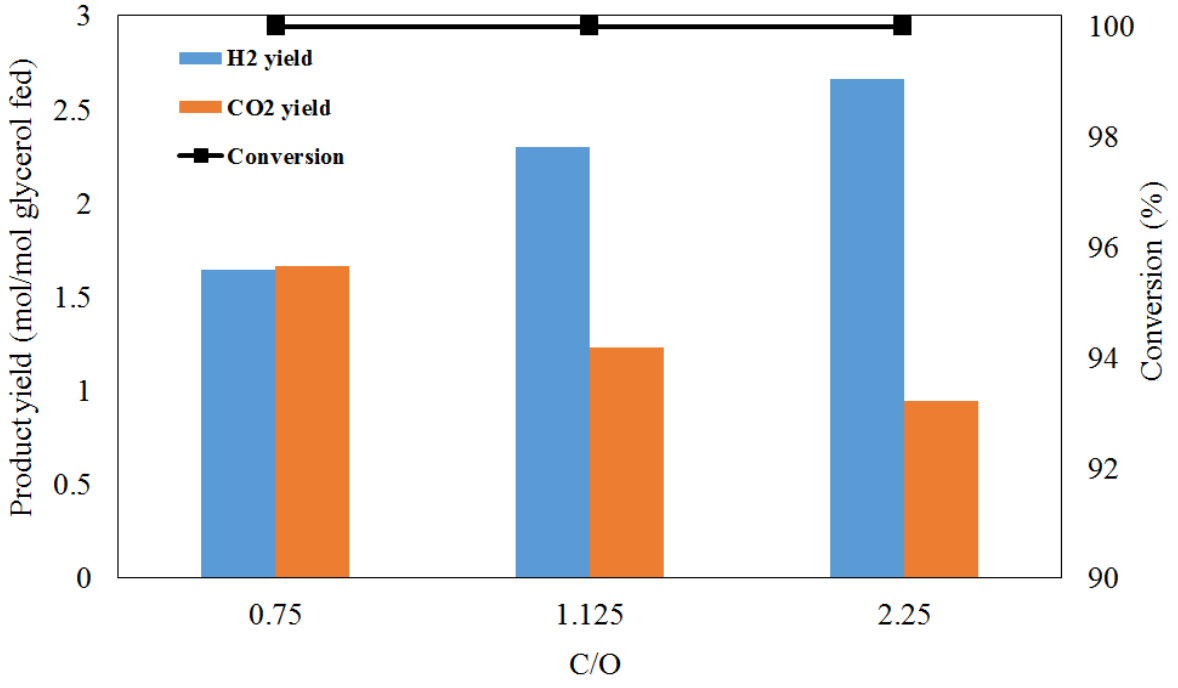

Figure 5.4. Effect of C/O on glycerol OSR at 700 °C.

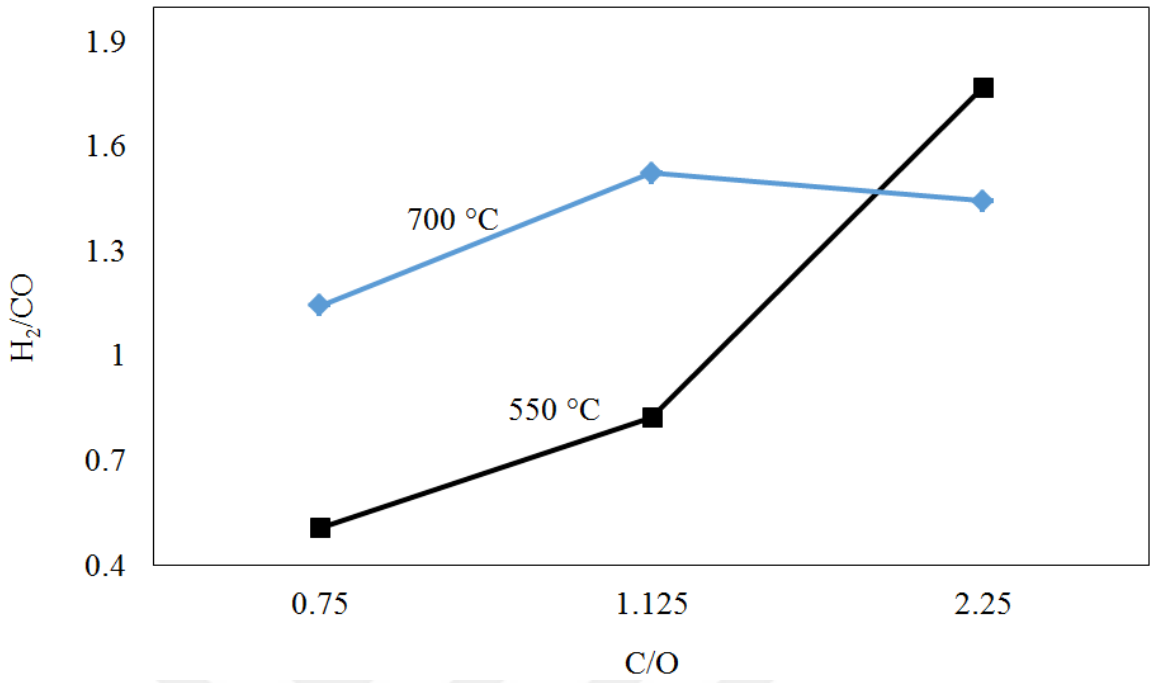

Figure 5.5. Effect of C/O on outlet H_2/CO ratio.

5.1.3. Effect of S/C on Glycerol Oxidative Steam Reforming

In order to investigate effect of S/C on glycerol oxidative steam reforming, experiments were conducted at 550 °C and 700 °C and S/C range of 3-4 (Table 5.3 and Figures 5.6-5.8). S/C in the studied range is found to have an insignificant effect on glycerol reforming as compared to temperature and C/O effects.

Table 5.3. Product yields over S/C range of 3-5 at C/O of 1.125 and two temperatures (550 °C and 700 °C).

Temperature (°C)	**S/C**	**Conversion (%)**	**Product Yields (mol/mol glycerol fed)(×10)**				
			H_2	**CH_4**	**CO**	**CO_2**	**C_{1+}**
550	3	100	11.0	1.3	20.6	6.3	1.1
	4	100	13.2	1.4	17.7	7.8	1.5
	5	93.4	13.7	1.3	16.5	8.2	1.0
700	3	100	20.7	1.5	22.1	8.9	0.7
	4	100	22.6	1.7	19.0	11.7	1.1
	5	100	23.0	1.7	15.4	12.3	0.9
700 (blank)	3	100	13.1	2.2	21.6	5.4	9.5

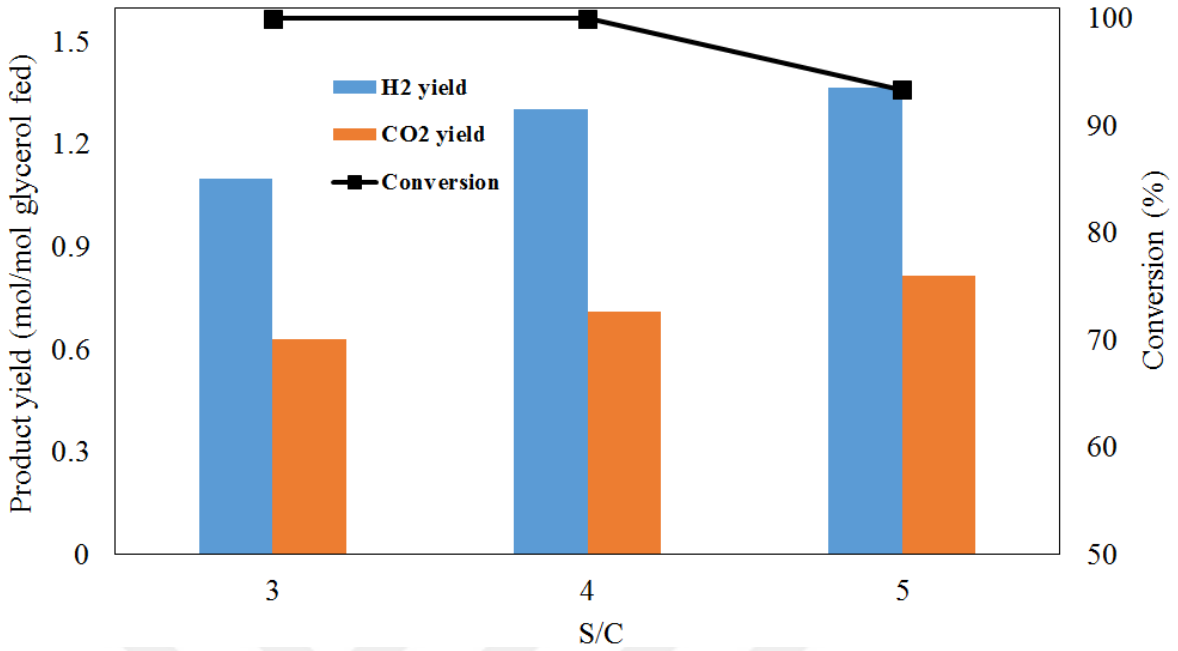

Figure 5.6. Effect of S/C on glycerol OSR at 550 °C.

At both temperatures, it is observed that conversion increased when steam content of feed is increased. This could be due to the coke gasification (Reaction 5.3) which becomes effective under reaction conditions. Coke removal results in an increase in the amount of gaseous carbon containing species which contributes to glycerol conversion. The increase in CO yield can be attributed to the WGS reaction as it consumes CO, which is generated via glycerol decomposition (Reaction 1.2), and generated CO_2 and H_2. An observation that may confirm this hypothesis is the correlation between the fact that WGS is favored at lower temperature and having more responsive CO_2 and H_2 yields at 550 °C (Figure 5.6) as compared to 700 °C (Figure 5.7). By raising S/C from 3 to 5 at 550 °C, H_2 and CO_2 yields increased by 12.3% and 44.1%, respectively; however, there was 9% elevation in H_2 yield and 33.5% in CO_2 yield at 700 °C. CH_4 and C_{1+} yields do not show a clear trend and were not as responsive as H_2 and CO_2. H_2/CO ratio increased with both S/C and temperature (Figure 5.8). This shows that product stream is tunable towards desired H_2/CO ratio and it can be achieved by suitably setting the conditions including temperature, S/C and C/O. The blank test shown in Table 5.3 shows that at low S/C ratios, the catalyst still is able to affect the product distribution pattern significantly confirming that the possible coke deposition at low steam content feed did not reduce the catalyst activity.

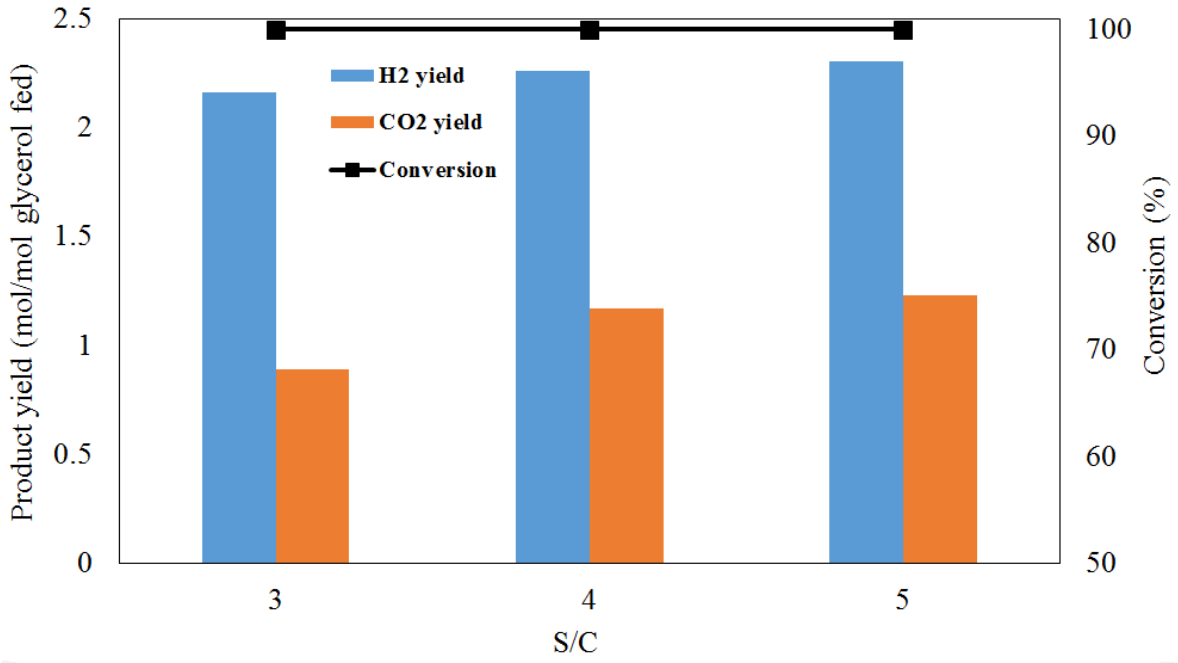

Figure 5.7. Effect of S/C on glycerol OSR at 700 °C.

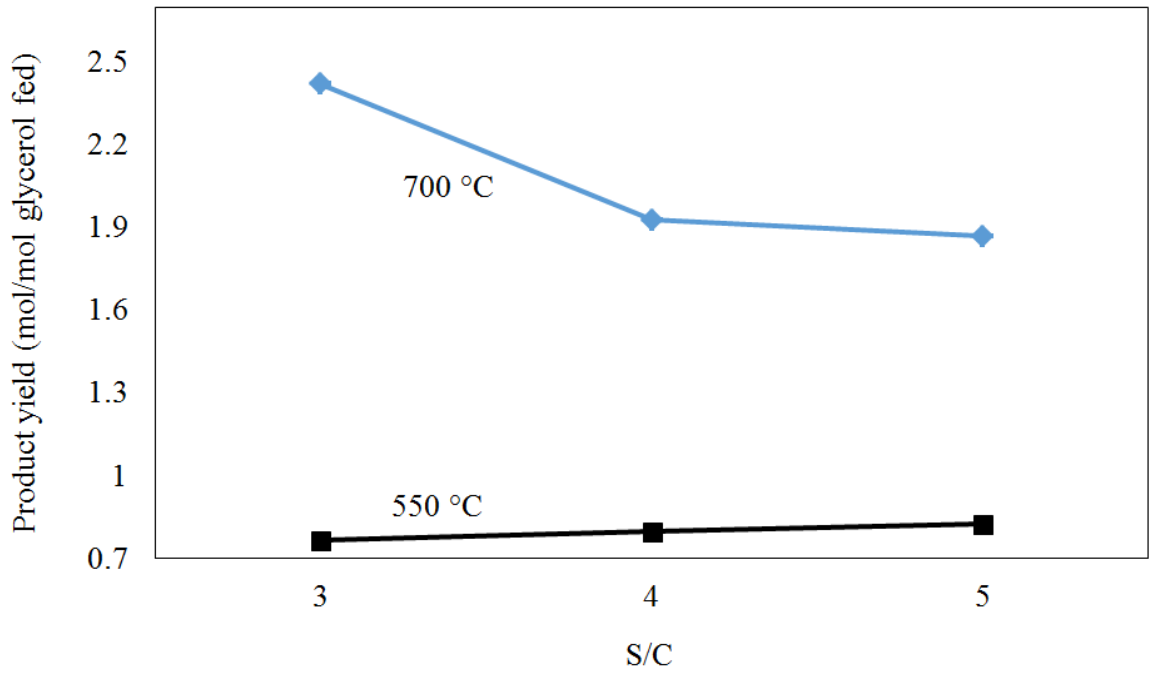

Figure 5.8. Effect of S/C on outlet H_2/CO ratio.

5.2. Modeling of Glycerol Steam Reforming in a Heat-Exchange Integrated Microchannel Reactor

This section provides the outcomes of the parametric study and the discussion of the results which are expressed in terms of glycerol conversion and temperature distribution along the line of symmetry (i.e. centerline) of the reforming channel (Figure 4.1). Glycerol conversion is defined as the ratio of the number of moles of glycerol consumed in Reaction 1.1 to the number of moles of glycerol fed into the reforming channel, and is reported in Table 5.4 for all parametric combinations studied. It is assumed that glycerol is pure, and the effluent stream is composed of a mixture of unconverted glycerol, excess steam, inert N_2, H_2, CO, CO_2 and CH_4 according to Reactions 1.2, 1.3 and 4.1. Distribution of the products, H_2, CO, CO_2, and CH_4, is quantified in terms of their per cent selectivity defined below where $F_{i,\,out}$ is outlet flow rate if species *i* [99]:

$$S_i = \frac{F_{i,\,out}}{F_{H2,\,out} + F_{CO2,\,out} + F_{CO,\,out}F_{i,\,out} + F_{CH4,\,out}} \tag{5.5}$$

5.2.1. Effect of S/C

The effect of S/C, which is varied from 1 to 6, on the product selectivity is presented Table 5.4. Glycerol conversion is found to increase from 65.1% at S/C of 1 to 75.3% at S/C of 6 due to elevated rate of glycerol decomposition with the higher amount of steam in the feed. Figure 5.9 shows the impact of S/C on product selectivity. H_2 selectivity is found to be the least responsive to S/C, as it slightly increased from 64.4% to 64.8% by raising S/C from 1 to 6, giving an average H_2 selectivity of 64.7%. The selectivity towards CO_2 is also weakly affected by S/C, given that it increased from 20.3% to only 21.7%. Increase in H_2 and CO_2 selectivities can be attributed to the WGS reaction whose rate enhances with S/C as order of reaction with respect to steam is higher than that of glycerol. As a result of higher rate of WGS reaction at higher S/C, selectivity towards CO decreases from 12.8% to 10.8%, showing that CO selectivity is the most responsive to S/C. Within the whole range of S/C, selectivity towards CH_4 is found to be less than 2.7% which is attributed to the high activation energy of Reaction 4.1 that is about two times as high as that of WGS and glycerol decomposition reactions.

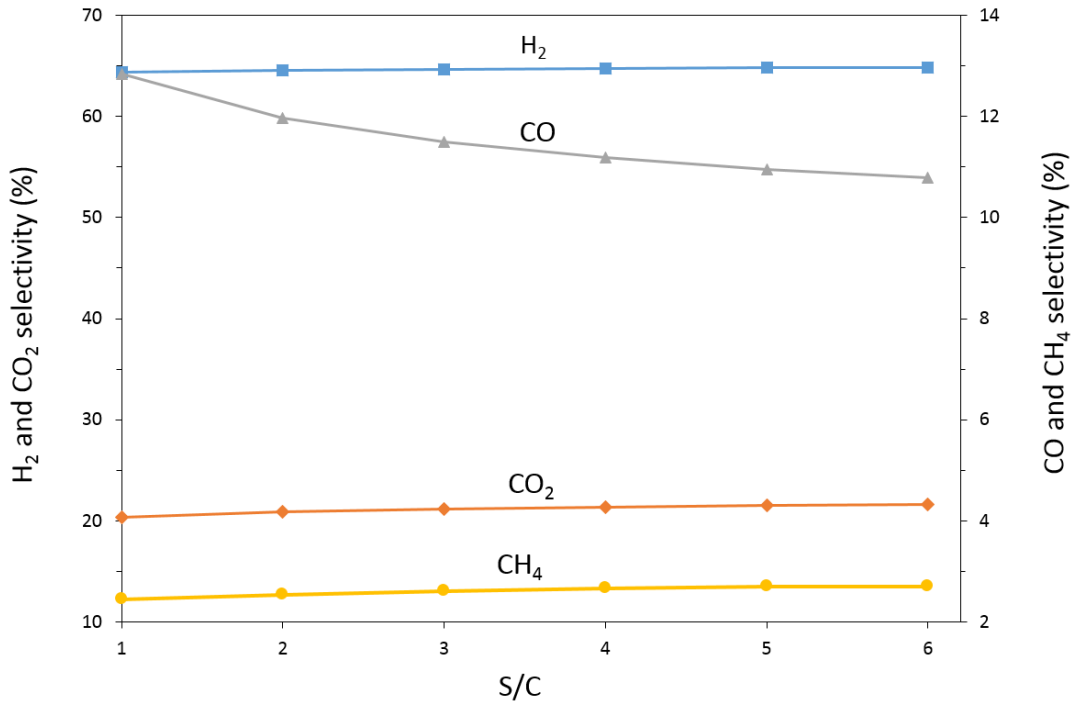

Figure 5.9. Effect of S/C on the selectivities towards H_2, CO_2, CO and CH_4.

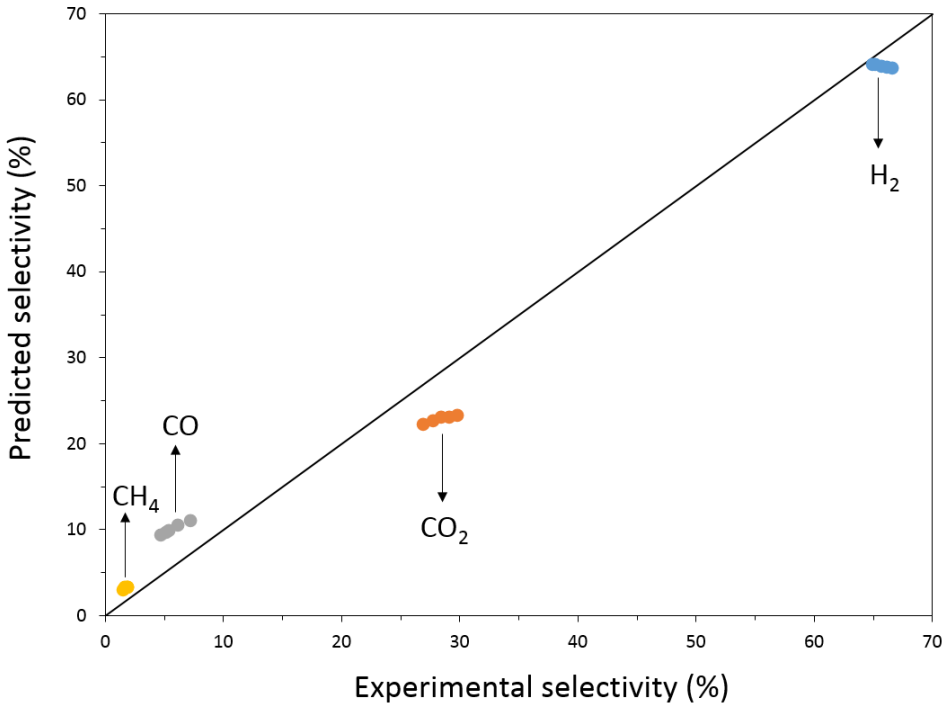

Figure 5.10. Parity plot for product selectivities at 823 K and S/C between 1.14 and 3.98 (experimental selectivities taken from Ref. [5]).

The effect of S/C on product distribution is also investigated by Cheng *et al.* [5] for the S/C range of 1.14 to 3.98 at temperature of 823 K and GHSV of 5.0×10^4 $mL.g_{cat}^{-1}.h^{-1}$ in a microreactor containing bimetallic Co-Ni/Al_2O_3 catalyst. In order to ensure the validity of the assumptions underlying the model, comparison between the experimental selectivities and those predicted by the model solved under the conditions employed by Cheng *et al.* [5] are presented in Figure 5.10. The parity plot indicates that the model predictions are in good agreement with their experimental counterparts.

5.2.2. Effect of Flow Configuration

The effect of flow direction of steam with respect to the reactive mixture is presented in Table 5.4 and in Figure 5.11 in terms of glycerol conversion and of temperature distribution in the reforming channel, respectively. The results show that changing the flow configuration from counter-current to co-current configuration does not have a significant impact on the reactor operation. The slightly better performance of co-current flow partitioning can be explained by the fact that maximum steam heating is supplied when the reaction, and subsequent heat consumption, is at its highest rate. This fact is reflected to the evolution of temperature that is found to decrease faster in the counter-current configuration till 3.5×10^{-3} m from the reforming channel inlet. In the next 1.5×10^{-3} m zone, the introduced steam results in re-increasing the temperature in the counter-current configuration, compensating for the slower reaction rate within the first 3.5×10^{-3} m zone. These two counteracting phenomena lead to almost equal glycerol conversions and same product distribution obtained from counter- and co-current configurations.

The results also reveal the significance of heat exchange integration in glycerol reforming. The maximum temperature drop along the reforming channel centerline is 56 K for counter-current and co-current configurations, while it is 135 K under the adiabatic conditions, which do not involve heating by steam (Figure 5.11). The importance of heating is not only visible by the temperature profiles, but also reflected to the glycerol conversions, which decreased by ~10% when no steam heating is provided (Table 5.4). Considering the endothermic nature of glycerol SR, the reaction is favored both kinetically and thermodynamically at higher temperatures leading to improved glycerol conversions.

Steam heating also affects product distribution, as it increases H_2 selectivity by 0.2% and suppresses the selectivity towards CH_4 from 3.1% to 2.7%. These findings emphasizes the importance of integrating heat-exchange function to a microchannel reactor for improving the performance via regulating temperature of the reaction channel, which is also mentioned in the literature [84-86, 100, 101]. It is worth noting that, the modeling approach presented in Ref. [71] is used to simulate the microchannel reactor without heating function.

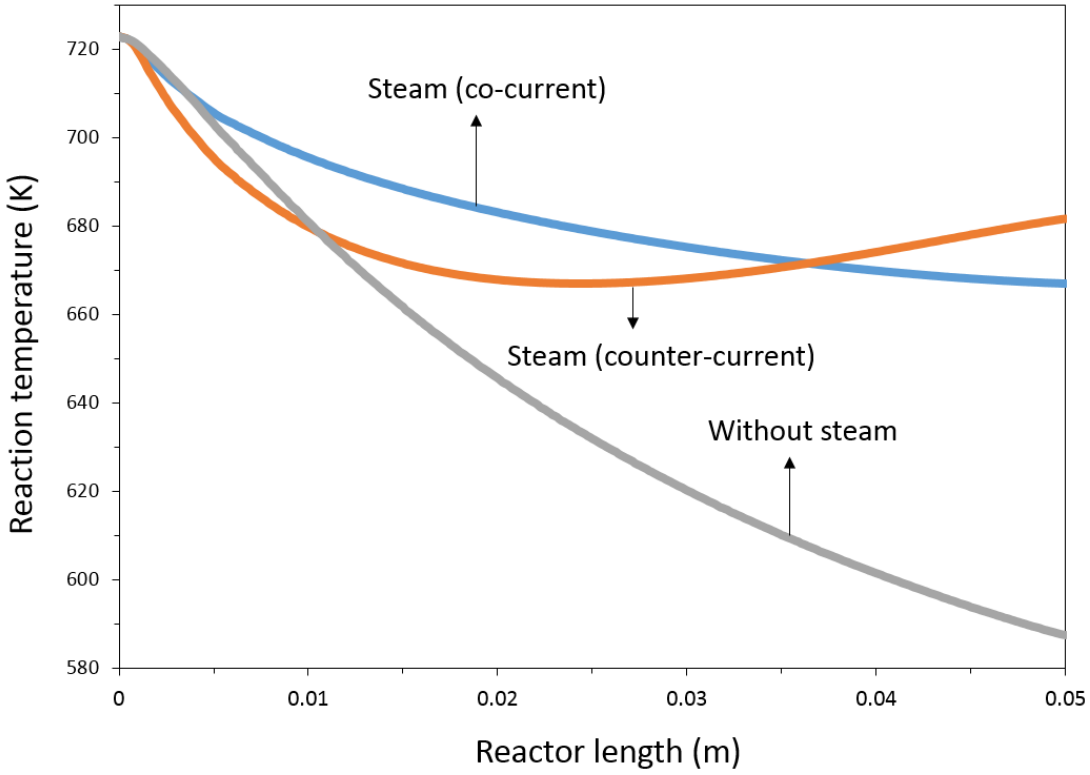

Figure 5.11. Effects of flow direction of steam and absence of steam heating on temperature of the reforming channel.

5.2.3. Effects of Inlet Temperatures of Reactive Mixture and Steam

The effects of inlet temperatures of the reactive mixture and steam on reactor performance are presented in Figures 5.12 and 5.13, and in Table 5.4. It is clearly observed that the feed temperature of reactive mixture has a significant impact on temperature distribution. This effect is reflected to glycerol conversion, which is found to increase from

66.9% to 78.6% upon changing the inlet temperature from 673 K to 773 K (Table 5.4). Such a change can be explained by the strong dependence of the reaction rate on temperature. It is worth noting that the impact of heating by steam, which is fed at 723 K, becomes more visible when the reactive mixture is fed at lower temperatures: the zones of endothermic temperature drop and heating-driven temperature rise are found to be narrower and wider, respectively (Figure 5.12). However, regardless of the feed values, the corresponding exit temperatures clustered below 700 K, i.e. in the range of 670 K-690 K.

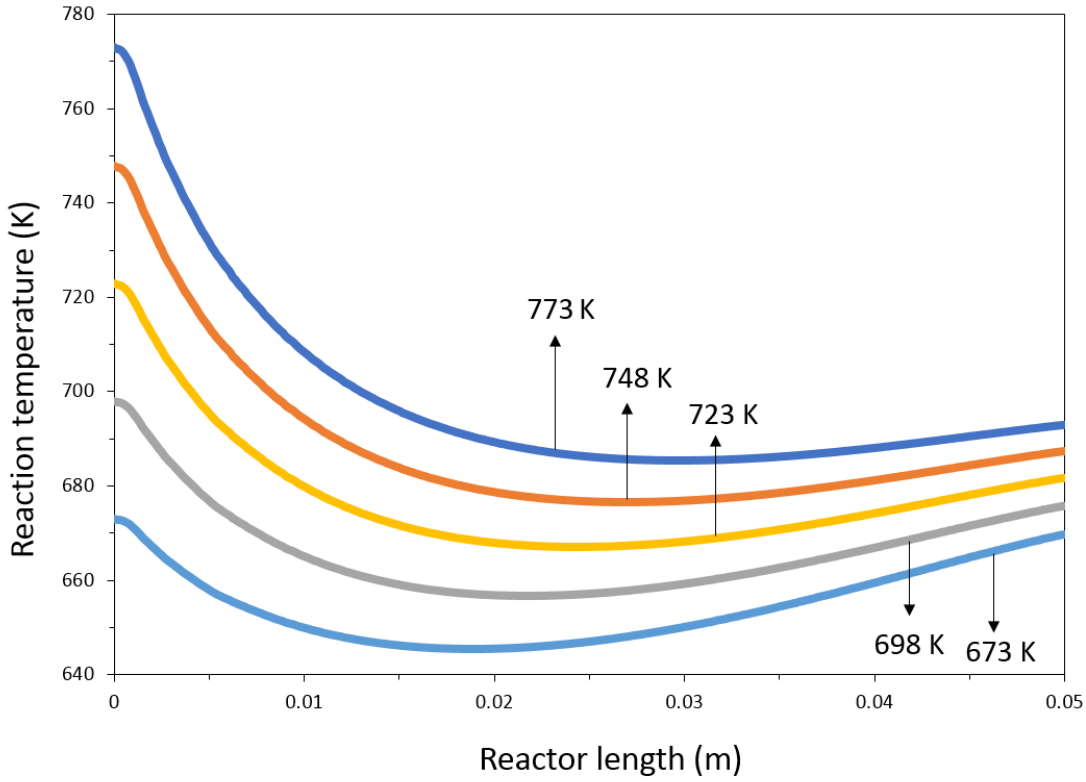

Figure 5.12. Effect of the inlet temperature of the glycerol vapor/steam mixture on temperature of the reforming channel. Simulated values of inlet temperature of the reactive mixture are presented in the figure.

The reflection of the change in the feed temperature of steam to the temperature profiles of the reforming channel is somewhat different (Figure 5.13). In these sets of simulations, reactive mixture is fed at 723 K, and temperature drop due to endothermic nature of the reaction is found to be common within ~5.0×10^{-3} m of the beginning of the catalyst layer. After this zone, however, the effect of steam inlet temperature is observed to

become significant. The resulting pattern of temperature profiles shown in Figure 5.13 is due to the counter-current flow configuration. The end effect of increasing steam inlet temperature from 663 K to 783 K is the subsequent change in conversion from 67.2% to 77.3% (Table 5.4). The temperature gradient within the reforming channel is also found to be a strong function of steam inlet temperature, as it decreased from 89 K to 31 K when steam inlet temperature is raised from 663 K to 783 K. The same effect is found to reduce CH_4 selectivity by 0.2%, suggesting its suppression with more uniform temperature distribution. This finding is in alignment with the increasing temperature gradient within the channel by higher inlet temperature of reactive mixture (Figure 5.12) that is found to elevate CH_4 selectivity from 2.3% at 673 K to 3.0% at 773 K, and to decrease H_2 selectivity from 65.0% to 64.5%.

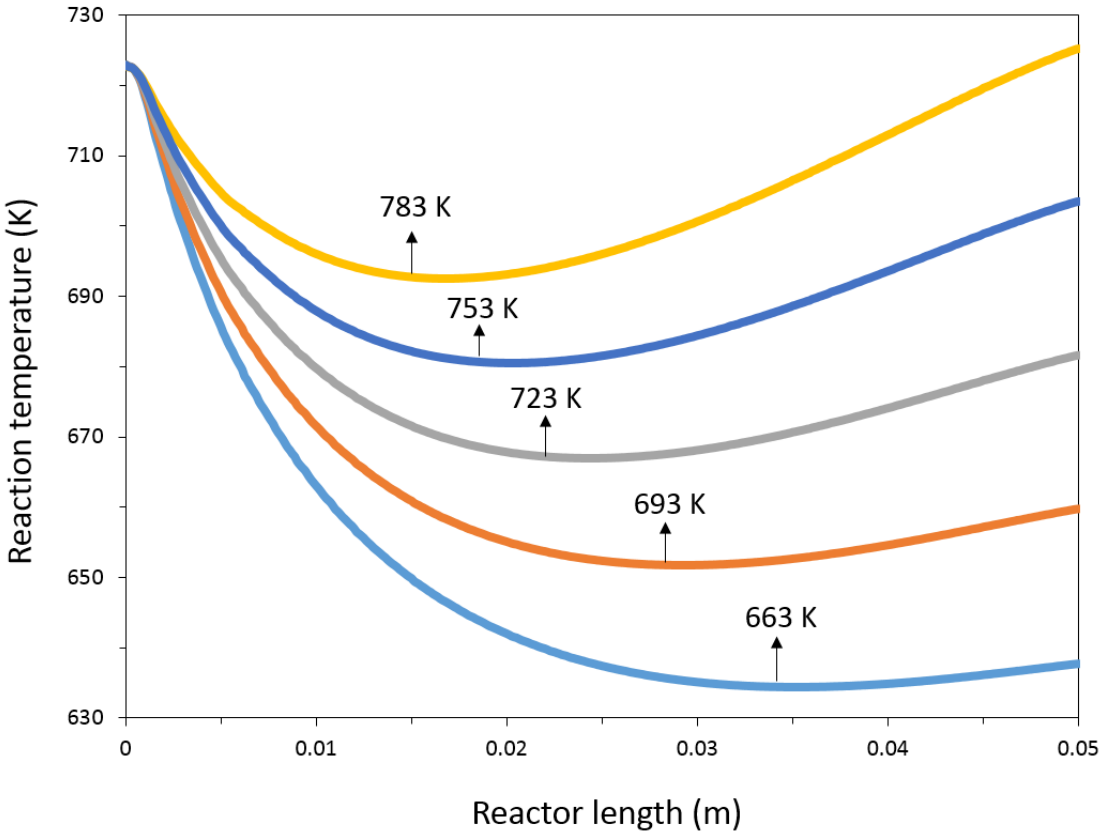

Figure 5.13. Effect of inlet temperature of steam on temperature of the reforming channel. Simulated values of inlet temperature of steam are presented in the figure.

5.2.4. Effect of Inlet Steam Velocity

The effect of inlet steam velocity on temperature distribution and on glycerol conversion/product selectivities is reported in Figure 5.14 and in Table 5.4, respectively. Increasing the inlet flow rate of steam from 2 $m.s^{-1}$ to 5 $m.s^{-1}$ is found to improve glycerol conversion by ~6% and to lead to a drop in the temperature gradient along the reforming channel from 81 K to 56 K while product distribution stays untouched.

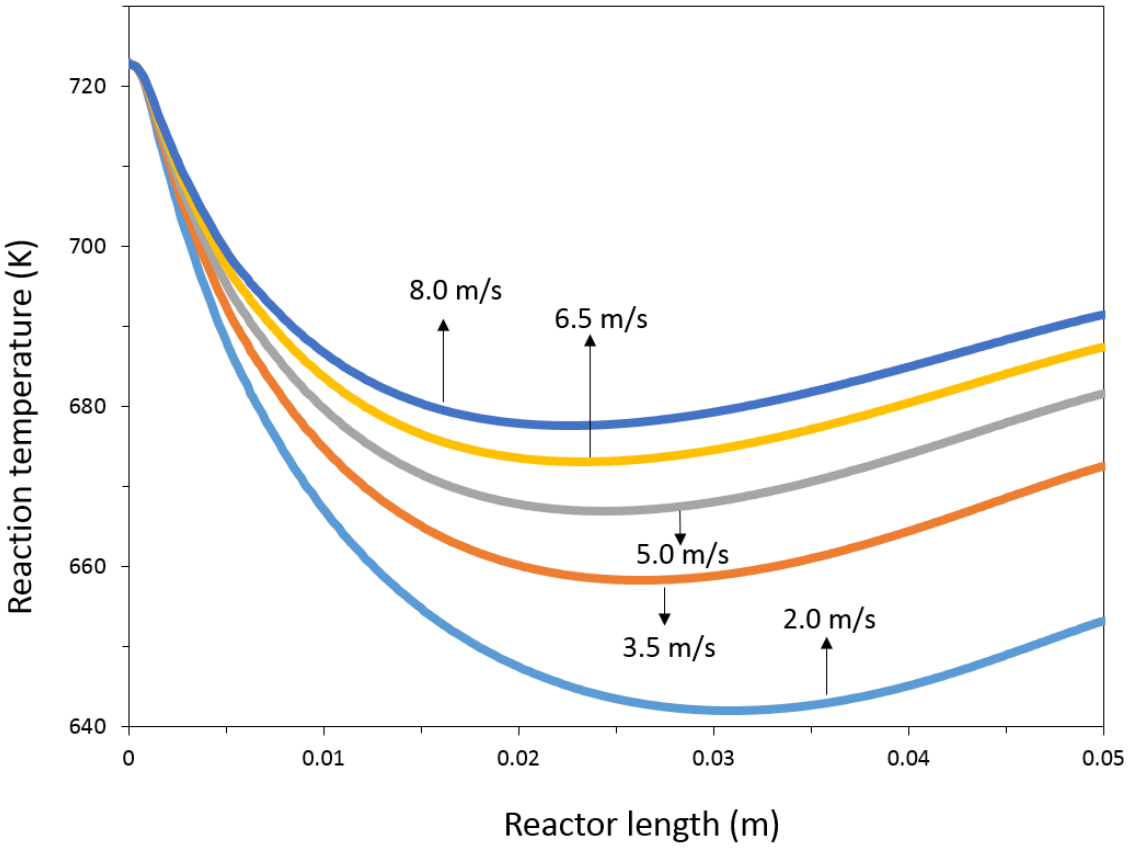

Figure 5.14. Effect of inlet velocity of steam on temperature of the reforming channel. Simulated values of steam inlet velocity are presented in the figure.

Even though these responses are desirable, the findings in Figure 5.14 show that the gaps between the profiles become smaller with further increase in steam inlet velocity (i.e. in the range of 5–8 $m.s^{-1}$). Feeding steam at higher linear velocities corresponds to higher mass flow rates, which increase the amount of sensible heat carried along the heating

channel. The same effect, on the other hand, causes the residence time of steam to decrease in the reactor and inherently reduces the extent of heating. These two contradicting phenomena are believed to hinder the impact of steam velocity when it exceeds 5 m/s. However, even at velocities higher than 5 $m.s^{-1}$, improvement in the heat transfer coefficient with steam velocity on the heating channel should not be overlooked [101]. Even though the flow is laminar, heat transfer coefficient can slightly increase with the flow rate [102], and lead to a minor improvement in heating effect of steam, which is in accordance with the magnitude of change in the reforming channel temperature (Figure 5.14) and in glycerol conversion (Table 5.4). Based on this observation, it can be stated that the effect of changing steam feed velocity from 2 $m.s^{-1}$ to 5 $m.s^{-1}$ on heating the reforming channel is more notable than the effect obtained in the range of 5–8 m/s. This point can be taken into account in determining the steam velocity which affects the cost of production of steam as a utility.

5.2.5. Effect of Reactor Material and Thickness of the Wall Separating Channels

The effect of thickness of the solid wall between reforming and heating channels on conversion and selectivities, and on temperature distribution is presented in Table 5.4 and in Figure 5.15, respectively. It is observed that changing the wall thickness from 4×10^{-4} m to 1.2×10^{-3} m does not affect product distribution. However, it causes an increase in conversion from 73.0% to 74.3%, and an 11 K reduction in temperature gradient occurring along the centerline of the reforming. This response is related to the temperature of the reforming channel that increased progressively with the wall thickness (Figure 5.15). The trends observed in Figure 5.15 reveal that reforming channel is heated somewhat more effectively when thicker walls are used. In the first half of the channel heat conduction in the axial direction (z-direction, Figure 4.1) becomes more notable and allows a more effective distribution of the sensible heat of the steam to the endothermic reforming reaction. Similar effect of wall thickness on temperature and heat flux distribution in heat-exchange integrated microchannel reactors is reported elsewhere [22, 26]. In the second half of the channel, however, decreasing values of wall thickness are found to give sharper elevations in temperature, leading to almost unified temperatures at the exit of the reforming channel. This suggests that at the second half of the channel, heating by steam starts to overcome the endothermicity of glycerol steam reforming. Considering the

counter-current flow configuration, the exit zone of the reactor is subject to heat exchange with the incoming steam, which is at its highest temperature. As axial heat conduction is less favored with wall thickness, normal component of heat flux becomes more intense at the inlet of the reactor with 4×10^{-4} m thick separating wall. The profiles presented in Figure 5.15 also show that, improvement in temperature distribution and subsequent increase in conversion become less pronounced with wall thickness. This statement can be verified by the fact that the gaps between the profiles get smaller with increasing wall thickness, which starts to act as a thicker physical barrier against heat conduction. Therefore, wall thickness needs to be optimized by considering the balance between the heat flux distribution and the barrier effect.

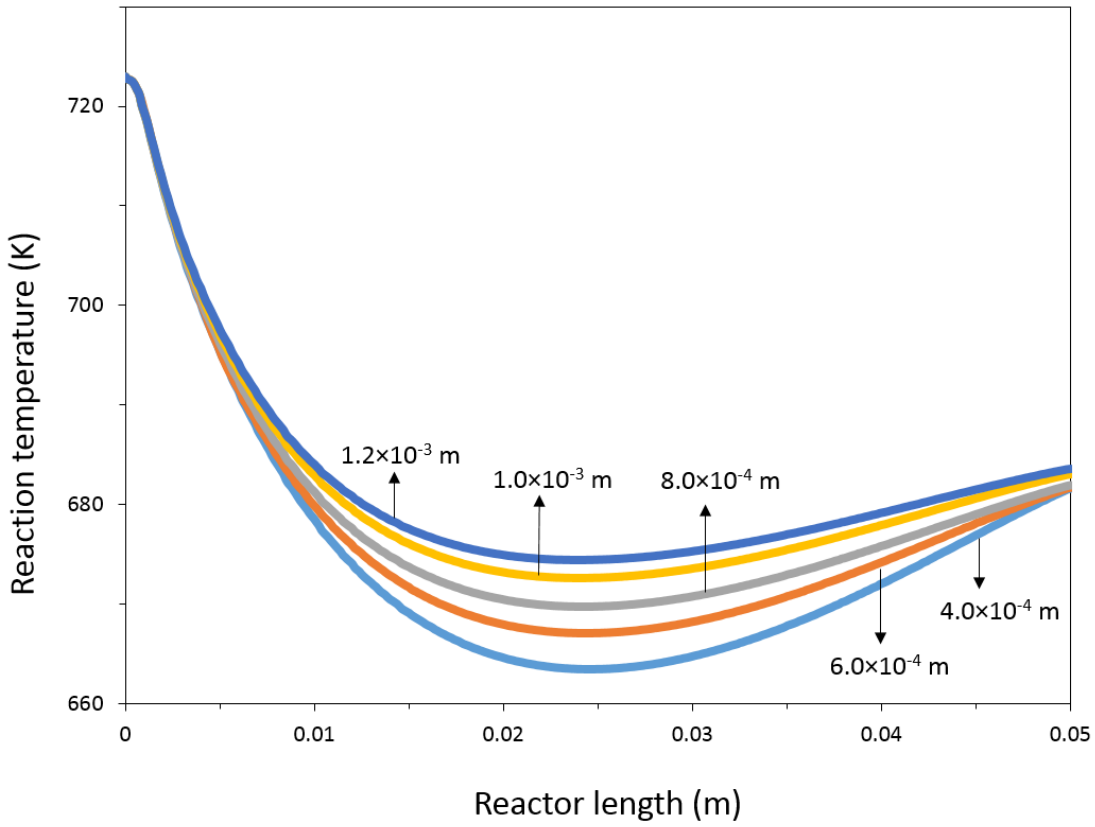

Figure 5.15. Effect of thickness of the wall separating reforming and heating channels on temperature of the reforming channel. Simulated wall thickness values are presented in the figure.

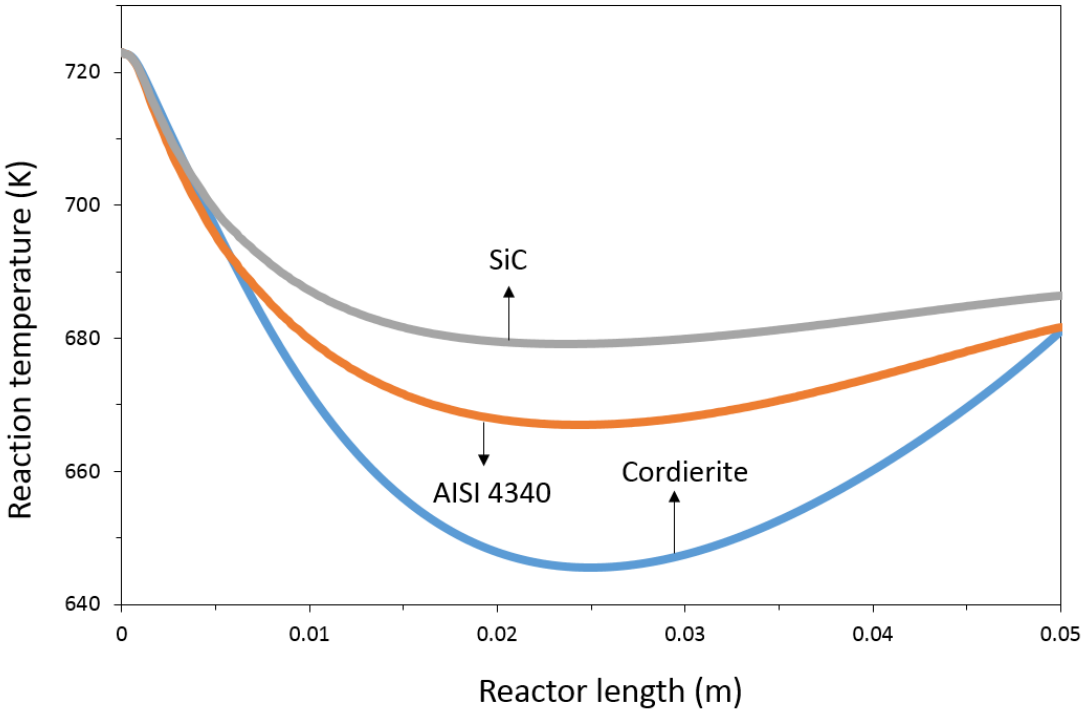

Figure 5.16. Effect of solid wall material on temperature of the reforming channel. Simulated wall materials are mentioned in the figure.

The impact of wall material, that is the material of construction of the microchannel reactor, on glycerol conversion, product distribution and temperature distribution is presented in Table 5.4 and in Figure 5.16. The materials, silicon carbide (SiC), AISI steel (4340 type) and cordierite, are selected on the basis of their availability and suitability for being used in microchannel reactor construction. The results show that uniformity of temperature distribution along the reforming channel and average channel temperature increase in the order of cordierite < AISI steel < SiC (Figure 5.16). Using SiC instead of cordierite gives 6.1% increase in glycerol conversion under identical operating conditions. This increase is found to be 2.5% when AISI steel is replaced with SiC. These trends can be linked to the difference in the thermal conductivity of the materials, which are 3 W/m.K for cordierite, 42 W/m.K for AISI steel and 120 W/m.K for SiC [103]. Thermal conductivity is an indication of fast delivery of the sensible heat of the steam to the reforming channel, and its increase improves distribution of axial (*z*-direction) component of heat flux to the reaction channel as explained elsewhere for different heat exchange integrated microreactor configurations [85, 86, 100]. Although it did not affect the product

distribution significantly, the quantitative outcome of this effect is reflected to the temperature gradient along the centerline, which decreased from 77 K to 56 K when AISI steel is used instead of cordierite (Figure 5.16). The gradient is found to be even smaller (44 K) in case of SiC.

Table 5.4. Glycerol conversions obtained at different structural and operational configurations; default values of the parameters are shown in italics.

Parameter	**Parameter value**	**Glycerol conversion (%)**	**S_{H_2} (%)**	**S_{CO} (%)**	**S_{CO_2} (%)**	**S_{CH_4} (%)**
S/C	1	65.1	64.4	12.8	20.3	2.5
	2	69.7	64.6	12.0	20.9	2.5
	3	71.9	64.7	11.5	21.2	2.6
	4	73.3	64.7	11.2	21.4	2.7
	5	74.4	64.8	10.9	21.6	2.7
	6	75.3	64.8	10.8	21.7	2.7
Direction of reactive flow and steam	*Counter-current*	73.3	64.7	11.2	21.4	2.7
	Co-current	74.3	64.7	11.2	21.4	2.7
	Without steam	63.8	64.5	11.0	21.4	3.1
Inlet temperature of steam (K)	663	67.2	64.7	11.2	21.3	2.8
	693	70.6	64.7	11.2	21.4	2.7
	723	73.3	64.7	11.2	21.4	2.7
	753	75.5	64.8	11.2	21.4	2.6
	783	77.3	64.8	11.2	21.4	2.6
Inlet temperature of the reactive mixture (K)	673	66.9	65.0	11.2	21.5	2.3
	698	70.3	64.9	11.2	21.4	2.5
	723	73.3	64.7	11.2	21.4	2.7
	748	76.1	64.6	11.2	21.4	2.8
	773	78.6	64.5	11.1	21.4	3.0

Table 5.4. Glycerol conversions obtained at different structural and operational configurations; default values of the parameters are shown in italics (cont.).

Parameter	**Parameter value**	**Glycerol conversion (%)**	**S_{H_2} (%)**	**S_{CO} (%)**	**S_{CO_2} (%)**	**S_{CH_4} (%)**
Inlet velocity of steam ($m.s^{-1}$)	2	69.0	64.7	11.2	21.4	2.7
	3.5	72.0	64.7	11.2	21.4	2.7
	5	73.3	64.7	11.2	21.4	2.7
	6.5	74.2	64.7	11.2	21.4	2.7
	8	74.8	64.7	11.2	21.4	2.7
Thickness of the wall between the channels (m)	4×10^{-4}	73.0	64.7	11.2	21.4	2.7
	6×10^{-4}	73.3	64.7	11.2	21.4	2.7
	8×10^{-4}	73.7	64.7	11.2	21.4	2.7
	1×10^{-3}	74.0	64.7	11.2	21.4	2.7
	1.2×10^{-3}	74.3	64.7	11.2	21.4	2.7
Reactor material	Cordierite	75.8	64.7	11.2	21.4	2.7
	AISI Steel	73.3	64.7	11.2	21.4	2.7
	Silicon Carbide (SiC)	69.7	64.8	11.2	21.4	2.6

6. CONCLUSIONS AND RECOMMENDATIONS

6.1. Conclusions

This study was composed of two parts including experimental and computational investigation of glycerol reforming. In the experimental part, glycerol oxidative reforming was conducted over a Rh/Al_2O_3 wall-coated microchannel reactor. The effect of parameters such as temperature, C/O and S/C on product distribution were of interest. The computational study aimed to understand the response of glycerol steam reforming in a microchannel reactor involving integrated steam heating function by means of a parametric study of investigating effects of structural parameters and operating conditions on temperature of the reforming channel and on glycerol conversion are explored. Major conclusions of study are as follows:

6.1.1. Experimental Part Conclusions

- Glycerol conversion increased with temperature due to the endothermic nature of glycerol decomposition
- Complete glycerol conversion was obtained over the temperature range of 600-700 °C at C/O of 1.125.
- S/C had much less effect on the glycerol OSR in terms of conversion and product distribution as compared to C/O and temperature.
- Conversion and H_2 yield slightly increased with steam content of the feed possibly via WGS and coke gasification.
- Decreasing C/O ratio improves conversion, but reduces H_2 yield.
- H_2/CO was found to be tunable through changing C/O, S/C and temperature.

6.1.2. Computational Part Conclusions

- In the S/C range of 1 to 6, the average selectivities towards H_2 and CO_2, CO and CH_4 were found to be in accordance with the experimental findings reported in the literature.

- Heat-exchange integrated operation was found to be superior to the one lacking steam heating.
- Reactor response remained almost unaffected by changing the reactive mixture–steam flow partitioning from counter-current to co-current configuration.
- Glycerol conversion has a strong dependence on and positively correlated with the inlet temperatures of steam and reactive mixture. On the other hand, inlet velocity of steam has a less profound effect on the reaction temperature and glycerol conversion.
- Use of thicker separating walls made of thermally conductive materials is found to favor heat flow into the reforming channel, which in turn elevates reaction temperature and conversion.
- Uniformity of temperature in the reaction channel favors the production of H_2 over CH_4.

6.2. Recommendations

Based on the reported results, the following recommendations might be worth of consideration in the future works:

- The effect of injector type and configuration can be investigated more deeply.
- Different reactor material can be examined to improve heat transfer within the catalyst bed.
- Other catalyst supports and active precious metal might be worth of investigation to optimize catalytic activity.
- Other reactor types such as fixed bed microchannel can be examined to compare its efficiency to the current microchannel configuration.
- Heat transfer between reaction and steam channel can be improved by modifying configuration of heat-exchange integrated reactors. A reactor with cross-flow configuration can be also worth of investigation.

REFERENCES

1. Van Gerpen, J., "Biodiesel processing and production", *Fuel Processing Technology*, Vol. 86, No. 10, pp. 1097-1107, 2005.

2. Meher, L., D. V. Sagar and S. Naik, "Technical aspects of biodiesel production by transesterification-a review", *Renewable And Sustainable Energy Reviews*, Vol. 10, No. 3, pp. 248-268, 2006.

3. Lin, Y.-C., "Catalytic valorization of glycerol to hydrogen and syngas", *International Journal of Hydrogen Energy*, Vol. 38, No. 6, pp. 2678-2700, 2013.

4. Delparish, A. and A. K. Avci, "Intensified catalytic reactors for Fischer-Tropsch synthesis and for reforming of renewable fuels to hydrogen and synthesis gas", *Fuel Processing Technology*, Vol. 151, pp. 72-100, 2016.

5. Cheng, C. K., S. Y. Foo and A. A. Adesina, "Glycerol steam reforming over bimetallic Co− Ni/Al_2O_3", *Industrial & Engineering Chemistry Research*, Vol. 49, No. 21, pp. 10804-10817, 2010.

6. Yang, G., H. Yu, F. Peng, H. Wang, J. Yang and D. Xie, "Thermodynamic analysis of hydrogen generation via oxidative steam reforming of glycerol", *Renewable Energy*, Vol. 36, No. 8, pp. 2120-2127, 2011.

7. Aasberg-Petersen, K., T. Christensen, I. Dybkjaer, J. Sehested, M. Østberg, R. Coertzen, M. Keyser and A. Steynberg, "Synthesis gas production for FT synthesis", *Studies in Surface Science and Catalysis*, Vol. 152, pp. 258-405, 2004.

8. Aasberg-Petersen, K., T. S. Christensen, C. S. Nielsen and I. Dybkjær, "Recent developments in autothermal reforming and pre-reforming for synthesis gas

production in GTL applications", *Fuel Processing Technology*, Vol. 83, No. 1, pp. 253-261, 2003.

9. Onsan, Z. I. and A. Avci, "Reactor design for fuel processing", *Fuel cells: technologies for fuel processing*, pp. 451-516, 2011.

10. Kiwi-Minsker, L. and A. Renken, "Microstructured reactors for catalytic reactions", *Catalysis Today*, Vol. 110, No. 1, pp. 2-14, 2005.

11. Kolb, G. and V. Hessel, "Micro-structured reactors for gas phase reactions", *Chemical Engineering Journal*, Vol. 98, No. 1, pp. 1-38, 2004.

12. Wu, C., V. Dupont, M. A. Nahil, B. Dou, H. Chen and P. T. Williams, "Investigation of Ni/SiO 2 catalysts prepared at different conditions for hydrogen production from ethanol steam reforming", *Journal of the Energy Institute*, 2016.

13. Ji, C., X. Dai, B. Ju, S. Wang, B. Zhang, C. Liang and X. Liu, "Improving the performance of a spark-ignited gasoline engine with the addition of syngas produced by onboard ethanol steaming reforming", *International Journal of Hydrogen Energy*, Vol. 37, No. 9, pp. 7860-7868, 2012.

14. Carvalho, F. L., Y. J. Asencios, J. D. Bellido and E. M. Assaf, "Bio-ethanol steam reforming for hydrogen production over Co_3O_4/CeO_2 catalysts synthesized by one-step polymerization method", *Fuel Processing Technology*, Vol. 142, pp. 182-191, 2016.

15. Ma, H., L. Zeng, H. Tian, D. Li, X. Wang, X. Li and J. Gong, "Efficient hydrogen production from ethanol steam reforming over La-modified ordered mesoporous Ni-based catalysts", *Applied Catalysis B: Environmental*, Vol. 181, pp. 321-331, 2016.

16. Navarro, R., M. Alvarez-Galvan, M. C. Sanchez-Sanchez, F. Rosa and J. G. Fierro, "Production of hydrogen by oxidative reforming of ethanol over Pt catalysts

supported on Al_2O_3 modified with Ce and La", *Applied Catalysis B: Environmental*, Vol. 55, No. 4, pp. 229-241, 2005.

17. Coronel, L., J. Múnera, A. Tarditi, M. Moreno and L. Cornaglia, "Hydrogen production by ethanol steam reforming over Rh nanoparticles supported on lanthana/silica systems", *Applied Catalysis B: Environmental*, Vol. 160, pp. 254-266, 2014.

18. Nozawa, T., Y. Mizukoshi, A. Yoshida and S. Naito, "Aqueous phase reforming of ethanol and acetic acid over TiO_2 supported Ru catalysts", *Applied Catalysis B: Environmental*, Vol. 146, pp. 221-226, 2014.

19. Sun, J., A. M. Karim, D. Mei, M. Engelhard, X. Bao and Y. Wang, "New insights into reaction mechanisms of ethanol steam reforming on Co–ZrO_2", *Applied Catalysis B: Environmental*, Vol. 162, pp. 141-148, 2015.

20. Youn, M. H., J. G. Seo, H. Lee, Y. Bang, J. S. Chung and I. K. Song, "Hydrogen production by auto-thermal reforming of ethanol over nickel catalysts supported on metal oxides: effect of support acidity", *Applied Catalysis B: Environmental*, Vol. 98, No. 1, pp. 57-64, 2010.

21. Chen, L.-C. and S. D. Lin, "Effects of the pretreatment of CuNi/SiO_2 on ethanol steam reforming: Influence of bimetal morphology", *Applied Catalysis B: Environmental*, Vol. 148, pp. 509-519, 2014.

22. Andreev, D., V. Radaev, L. Makarshin, A. Gribovskii, V. Zaikovskii and V. Parmon, "Ethanol steam reforming over Co/ZnO and Rh/Al_2O_3 catalysts in a microchannel catalytic reactor", *Kinetics and Catalysis*, Vol. 55, No. 6, pp. 798-808, 2014.

23. Domínguez, M., G. Cristiano, E. López and J. Llorca, "Ethanol steam reforming over cobalt talc in a plate microreactor", *Chemical Engineering Journal*, Vol. 176, pp. 280-285, 2011.

24. Uriz, I., G. Arzamendi, E. López, J. Llorca and L. Gandía, "Computational fluid dynamics simulation of ethanol steam reforming in catalytic wall microchannels", *Chemical Engineering Journal*, Vol. 167, No. 2, pp. 603-609, 2011.

25. Men, Y., G. Kolb, R. Zapf, V. Hessel and H. Löwe, "Ethanol steam reforming in a microchannel reactor", *Process Safety and Environmental Protection*, Vol. 85, No. 5, pp. 413-418, 2007.

26. Görke, O., P. Pfeifer and K. Schubert, "Kinetic study of ethanol reforming in a microreactor", *Applied Catalysis A: General*, Vol. 360, No. 2, pp. 232-241, 2009.

27. Rahman, M. A., F. R. García-García and K. Li, "On-board H_2 generation by a catalytic hollow fibre microreactor for portable device applications", *Catalysis Communications*, Vol. 16, No. 1, pp. 128-132, 2011.

28. Peela, N. R. and D. Kunzru, "Oxidative steam reforming of ethanol over Rh based catalysts in a micro-channel reactor", *International Journal of Hydrogen Energy*, Vol. 36, No. 5, pp. 3384-3396, 2011.

29. Cai, W., F. Wang, A. Van Veen, C. Descorme, Y. Schuurman, W. Shen and C. Mirodatos, "Hydrogen production from ethanol steam reforming in a micro-channel reactor", *International Journal of Hydrogen Energy*, Vol. 35, No. 3, pp. 1152-1159, 2010.

30. Peela, N. R., A. Mubayi and D. Kunzru, "Steam reforming of ethanol over $Rh/CeO_2/Al_2O_3$ catalysts in a microchannel reactor", *Chemical Engineering Journal*, Vol. 167, No. 2, pp. 578-587, 2011.

31. Peela, N. R. and D. Kunzru, "Steam reforming of ethanol in a microchannel reactor: kinetic study and reactor simulation", *Industrial & Engineering Chemistry Research*, Vol. 50, No. 23, pp. 12881-12894, 2011.

32. Bruschi, Y. M., E. López, N. S. Schbib, M. N. Pedernera and D. O. Borio, "Theoretical study of the ethanol steam reforming in a parallel channel reactor", *International Journal of Hydrogen Energy*, Vol. 37, No. 19, pp. 14887-14894, 2012.

33. Anzola, A. M., Y. M. Bruschi, E. López, N. S. Schbib, M. N. Pedernera and D. O. Borio, "Heat supply and hydrogen yield in an ethanol microreformer", *Industrial & Engineering Chemistry Research*, Vol. 50, No. 5, pp. 2698-2705, 2010.

34. Divins, N. J., E. López, Á. Rodríguez, D. Vega and J. Llorca, "Bio-ethanol steam reforming and autothermal reforming in 3-μm channels coated with $RhPd/CeO_2$ for hydrogen generation", *Chemical Engineering and Processing: Process Intensification*, Vol. 64, pp. 31-37, 2013.

35. Llorca, J., A. Casanovas, T. Trifonov, A. Rodríguez and R. Alcubilla, "First use of macroporous silicon loaded with catalyst film for a chemical reaction: A microreformer for producing hydrogen from ethanol steam reforming", *Journal of Catalysis*, Vol. 255, No. 2, pp. 228-233, 2008.

36. Casanovas, A., M. Domínguez, C. Ledesma, E. López and J. Llorca, "Catalytic walls and micro-devices for generating hydrogen by low temperature steam reforming of ethanol", *Catalysis Today*, Vol. 143, No. 1, pp. 32-37, 2009.

37. Tilland, A., J.-F. Portha, L. Falk and C. Tardivat, "Impact of reducing the channel diameter on heterogeneous gas reactions in an isothermal monolith", *Chemical Engineering and Processing: Process Intensification*, Vol. 95, pp. 317-326, 2015.

38. López, E., A. Irigoyen, T. Trifonov, A. Rodríguez and J. Llorca, "A million-channel reformer on a fingertip: moving down the scale in hydrogen production", *International Journal of Hydrogen Energy*, Vol. 35, No. 8, pp. 3472-3479, 2010.

39. Pla, D., M. Salleras, I. Garbayo, A. Morata, N. Sabaté, N. Divins, J. Llorca and A. Tarancón, "Fabrication and characterization of a fuel flexible micro-reformer fully

integrated in silicon for micro-solid oxide fuel cell applications", *SPIE Microtechnologies*, International Society for Optics and Photonics, 2015.

40. Fleisch, T., A. Basu, M. Gradassi and J. Masin, "Dimethyl ether: a fuel for the 21st century", *Studies in Surface Science and Catalysis*, Vol. 107, pp. 117-125, 1997.

41. Takeishi, K. and Y. Akaike, "Hydrogen production by dimethyl ether steam reforming over copper alumina catalysts prepared using the sol–gel method", *Applied Catalysis A: General*, Vol. 510, pp. 20-26, 2016.

42. Oar-Arteta, L., A. Remiro, A. T. Aguayo, M. Olazar, J. Bilbao and A. G. Gayubo, "Development of a bifunctional catalyst for dimethyl ether steam reforming with $CuFe_2O_4$ spinel as the metallic function", *Journal of Industrial and Engineering Chemistry*, Vol. 36, pp. 169-179, 2016.

43. Lü, J., S. Zhou, K. Ma, M. Meng and Y. Tian, "The effect of P modification on the acidity of HZSM-5 and P-HZSM-5/CuO-ZnO-Al_2O_3 mixed catalysts for hydrogen production by dimethyl ether steam reforming", *Chinese Journal of Catalysis*, Vol. 36, No. 8, pp. 1295-1303, 2015.

44. Zhang, L., M. Meng, S. Zhou, Z. Sun, J. Zhang, Y. Xie and T. Hu, "Promotional effect of Partial substitution of Zn by Ce in CuZnAlO catalysts used for hydrogen production via steam reforming of dimethyl ether", *Journal of Power Sources*, Vol. 232, pp. 286-296, 2013.

45. Mihai, O., A. Fathali, X. Auvray and L. Olsson, "DME, propane and CO: The oxidation, steam reforming and WGS over Pt/Al_2O_3. The effect of aging and presence of water", *Applied Catalysis B: Environmental*, Vol. 160, pp. 480-491, 2014.

46. Ledesma, C., U. S. Ozkan and J. Llorca, "Hydrogen production by steam reforming of dimethyl ether over Pd-based catalytic monoliths", *Applied Catalysis B: Environmental*, Vol. 101, No. 3, pp. 690-697, 2011.

47. Kruger, J. S., D. C. Rennard, T. R. Josephson and L. D. Schmidt, "Effect of Functional Groups on Autothermal Partial Oxidation of Bio-oil. Part 1: Role of Catalyst Surface and Molecular Oxygen", *Energy & Fuels*, Vol. 25, No. 7, pp. 3157-3171, 2011.

48. Ledesma, C. and J. Llorca, "Dimethyl ether steam reforming over Cu–Zn–Pd/CeO_2–ZrO_2 catalytic monoliths. The role of Cu species on catalyst stability", *The Journal of Physical Chemistry C*, Vol. 115, No. 23, pp. 11624-11632, 2011.

49. Ledesma, C. and J. Llorca, "Hydrogen production by steam reforming of dimethyl ether over Cu–Zn/CeO_2–ZrO_2 catalytic monoliths", *Chemical Engineering Journal*, Vol. 154, No. 1, pp. 281-286, 2009.

50. Ledesma, C., M. Domlnguez, N. Jimenez, E. Lopez and J. Llorca, "Hydrogen generation from renewables: Steam reforming of ethanol and dimethyl ether over structured catalysts", *Chimica oggi*, Vol. 27, No. 5, pp. 40-43, 2009.

51. Ledesma, C. and J. Llorca, "CuZn/ZrO_2 catalytic honeycombs for dimethyl ether steam reforming and autothermal reforming", *Fuel*, Vol. 104, pp. 711-716, 2013.

52. Yang, M., Y. Men, S. Li and G. Chen, "Hydrogen production by steam reforming of dimethyl ether over ZnO–Al_2O_3 bi-functional catalyst", *International Journal of Hydrogen Energy*, Vol. 37, No. 10, pp. 8360-8369, 2012.

53. Yang, M., Y. Men, S. Li and G. Chen, "Enhancement of catalytic activity over TiO_2-modified Al_2O_3 and ZnO–Cr_2O_3 composite catalyst for hydrogen production via dimethyl ether steam reforming", *Applied Catalysis A: General*, Vol. 433, pp. 26-34, 2012.

54. Zhang, Q., F. Fan, G. Xu, D. Ye, W. Wang and Z. Zhu, "Steam reforming of dimethyl ether over a novel anodic γ-Al_2O_3 supported copper bi-functional catalyst", *International Journal of Hydrogen Energy*, Vol. 38, No. 25, pp. 10305-10314, 2013.

55. Zhang, Q., J. Xu, F. Fan, D. Sun, G. Xu, S. Zhang and Z. Zhu, "Application of porous anodic alumina monolith catalyst in steam reforming of dimethyl ether: Cu/γ-Al_2O_3/Al catalyst degradation behaviors and catalytic activity improvement by pre-competition impregnation method", *Fuel Processing Technology*, Vol. 119, pp. 52-59, 2014.

56. Yu, B., K. Lee, K. Kim, D. J. Byun, H. Ha and J. Byun, "Partial oxidation of dimethyl ether using the structured catalyst Rh/Al_2O_3/Al prepared through the anodic oxidation of aluminum", *Journal of nanoscience and nanotechnology*, Vol. 11, No. 7, pp. 6298-6305, 2011.

57. Kim, D. H., S. H. Kim and J. Y. Byun, "A microreactor with metallic catalyst support for hydrogen production by partial oxidation of dimethyl ether", *Chemical Engineering Journal*, Vol. 280, pp. 468-474, 2015.

58. de Lucas-Consuegra, A., A. Calcerrada, A. De La Osa and J. Valverde, "Electrochemical reforming of ethylene glycol. Influence of the operation parameters, simulation and its optimization", *Fuel Processing Technology*, Vol. 127, pp. 13-19, 2014.

59. Wang, N., N. Perret and A. Foster, "Sustainable hydrogen production for fuel cells by steam reforming of ethylene glycol: A consideration of reaction thermodynamics", *International Journal of Hydrogen Energy*, Vol. 36, No. 10, pp. 5932-5940, 2011.

60. Izquierdo, U., M. Wichert, V. Barrio and G. Kolb, "Sustainable syngas production from ethylene glycol reforming processes using Rh-based catalysts in microreactors", *Applied Catalysis B: Environmental*, Vol. 152, pp. 19-27, 2014.

61. Izquierdo, U., M. Wichert, G. Kolb, V. Barrio, R. Zapf, A. Ziogas, S. Neuberg, P. Arias and J. Cambra, "Micro reactor hydrogen production from ethylene glycol reforming using Rh catalysts supported on CeO_2 and La_2O_3 promoted α-Al_2O_3", *International Journal of Hydrogen Energy*, Vol. 39, No. 10, pp. 5248-5256, 2014.

62. Dauenhauer, P., J. Salge and L. Schmidt, "Renewable hydrogen by autothermal steam reforming of volatile carbohydrates", *Journal of Catalysis*, Vol. 244, No. 2, pp. 238-247, 2006.

63. Kruger, J. S., D. C. Rennard, T. R. Josephson and L. D. Schmidt, "Effect of Functional Groups on Autothermal Partial Oxidation of Bio-oil. part 2: Role of homogeneous and support-mediated reactions", *Energy & Fuels*, Vol. 25, No. 7, pp. 3172-3185, 2011.

64. Kunkes, E. L., R. R. Soares, D. A. Simonetti and J. A. Dumesic, "An integrated catalytic approach for the production of hydrogen by glycerol reforming coupled with water-gas shift", *Applied Catalysis B: Environmental*, Vol. 90, No. 3, pp. 693-698, 2009.

65. Schwengber, C. A., H. J. Alves, R. A. Schaffner, F. A. da Silva, R. Sequinel, V. R. Bach and R. J. Ferracin, "Overview of glycerol reforming for hydrogen production", *Renewable and Sustainable Energy Reviews*, Vol. 58, pp. 259-266, 2016.

66. Wu, G., S. Li, C. Zhang, T. Wang and J. Gong, "Glycerol steam reforming over perovskite-derived nickel-based catalysts", *Applied Catalysis B: Environmental*, Vol. 144, pp. 277-285, 2014.

67. Slinn, M., K. Kendall, C. Mallon and J. Andrews, "Steam reforming of biodiesel by-product to make renewable hydrogen", *Bioresource Technology*, Vol. 99, No. 13, pp. 5851-5858, 2008.

68. Adhikari, S., S. Fernando and A. Haryanto, "Production of hydrogen by steam reforming of glycerin over alumina-supported metal catalysts", *Catalysis Today*, Vol. 129, No. 3, pp. 355-364, 2007.

69. Adhikari, S., S. Fernando and A. Haryanto, "Glycerin steam reforming for hydrogen production", *Transactions of the ASABE*, Vol. 50, No. 2, pp. 591-595, 2007.

70. Bobadilla, L., A. Álvarez, M. Domínguez, F. Romero-Sarria, M. Centeno, M. Montes and J. Odriozola, "Influence of the shape of Ni catalysts in the glycerol steam reforming", *Applied Catalysis B: Environmental*, Vol. 123, pp. 379-390, 2012.

71. Caglar, O. Y., C. D. Demirhan and A. K. Avci, "Modeling and design of a microchannel reformer for efficient conversion of glycerol to hydrogen", *International Journal of Hydrogen Energy*, Vol. 40, No. 24, pp. 7579-7585, 2015.

72. Park, D., C. Lee, D. J. Moon and T. Kim, "Novel Macro-micro Channel Reactor for Reforming Glycerol Produced from Biodiesel Productions", *Energy Procedia*, Vol. 61, pp. 2075-2078, 2014.

73. Liu, Y., R. Farrauto and A. Lawal, "Autothermal reforming of glycerol in a dual layer monolith catalyst", *Chemical Engineering Science*, Vol. 89, pp. 31-39, 2013.

74. Liu, Y. and A. Lawal, "Thermodynamic Analysis and Characterization of Syngas Production by Autothermal Reforming of Biodiesel Byproducts", *Energy Technology*, Vol. 2, No. 9-10, pp. 792-801, 2014.

75. Liu, Y. and A. Lawal, "Kinetic study of autothermal reforming of glycerol in a dual layer monolith catalyst", *Chemical Engineering and Processing: Process Intensification*, Vol. 95, pp. 276-283, 2015.

76. Rennard, D. C., J. S. Kruger and L. D. Schmidt, "Autothermal Catalytic Partial Oxidation of Glycerol to Syngas and to Non-Equilibrium Products", *ChemSusChem*, Vol. 2, No. 1, pp. 89-98, 2009.

77. Liu, S.-K. and Y.-C. Lin, "Generation of syngas through autothermal partial oxidation of glycerol over $LaMnO_3$ and $LaNiO_3$-coated monoliths", *Catalysis Today*, Vol. 237, pp. 62-70, 2014.

78. Liu, S.-K. and Y.-C. Lin, "Autothermal partial oxidation of glycerol to syngas over Pt-, LaMnO3-, and Pt/$LaMnO_3$-coated monoliths", *Industrial & Engineering Chemistry Research*, Vol. 51, No. 50, pp. 16278-16287, 2012.

79. Sadykov, V., N. Mezentseva, Y. Fedorova, A. Lukashevich, V. Pelipenko, V. Kuzmin, M. Simonov, A. Ishchenko, Z. Vostrikov and L. Bobrova, "Structured catalysts for steam/autothermal reforming of biofuels on heat-conducting substrates: Design and performance", *Catalysis Today*, Vol. 251, pp. 19-27, 2015.

80. Sadykov, V., N. Mezentseva, M. Simonov, E. Smal, M. Arapova, S. Pavlova, Y. Fedorova, O. Chub, L. Bobrova and V. Kuzmin, "Structured nanocomposite catalysts of biofuels transformation into syngas and hydrogen: Design and performance", *International Journal of Hydrogen Energy*, Vol. 40, No. 24, pp. 7511-7522, 2015.

81. Karakaya, M., S. Keskin and A. K. Avci, "Parametric study of methane steam reforming to syngas in a catalytic microchannel reactor", *Applied Catalysis A: General*, Vol. 411, pp. 114-122, 2012.

82. Avcı, A. K., D. L. Trimm, A. E. Aksoylu and Z. I. Önsan, "Hydrogen production by steam reforming of n-butane over supported Ni and Pt-Ni catalysts", *Applied Catalysis A: General*, Vol. 258, No. 2, pp. 235-240, 2004.

83. Aubin, J., L. Prat, C. Xuereb and C. Gourdon, "Effect of microchannel aspect ratio on residence time distributions and the axial dispersion coefficient", *Chemical Engineering and Processing: Process Intensification*, Vol. 48, No. 1, pp. 554-559, 2009.

84. Karakaya, M. and A. K. Avci, "Microchannel reactor modeling for combustion driven reforming of iso-octane", *International Journal of Hydrogen Energy*, Vol. 36, No. 11, pp. 6569-6577, 2011.

85. Karakaya, M. and A. K. Avci, “Simulation of on-board fuel conversion in catalytic microchannel reactor-heat exchanger systems”, *Topics in Catalysis*, Vol. 52, No. 13-20, pp. 2112-2116, 2009.

86. Tezcan, I. and A. K. Avci, “Parametric investigation of oxidative coupling of methane in a heat-exchange integrated microchannel reactor”, *Journal of Chemical Technology and Biotechnology*, Vol. 90, No. 10, pp. 1827-1838, 2015.

87. Wilke, C., “A viscosity equation for gas mixtures”, *The journal of chemical physics*, Vol. 18, No. 4, pp. 517-519, 1950.

88. Bird, R. B., W. E. Stewart and E. N. Lightfoot, *Transport Phenomena*, 2nd ed., John Wiley & Sons, New York, 2002.

89. Fuller, E. N., P. D. Schettler and J. C. Giddings, “New method for prediction of binary gas-phase diffusion coefficients”, *Industrial & Engineering Chemistry*, Vol. 58, No. 5, pp. 18-27, 1966.

90. Kapteijn, F. and J. Moulijn, *Laboratory testing of solid catalysts*, in *Handbook of heterogeneous catalysis*, Wiley-VCH, Weinheim, pp. 2019–2045, 2008.

91. Gregg, S. J., K. S. W. Sing and H. Salzberg, “Adsorption surface area and porosity”, *Journal of the Electrochemical Society*, Vol. 114, No. 11, pp. 279-281, 1967.

92. Perry, R. H. and D. W. Green, *Perry's Chemical Engineers' Handbook*., McGraw-Hill Professional, 1999.

93. Haynes, W. M., *CRC Handbook Of Chemistry and Physics*, CRC press, 2014.

94. Avcı, A. K., D. L. Trimm and M. Karakaya, “Microreactor catalytic combustion for chemicals processing”, *Catalysis Today*, Vol. 155, No. 1, pp. 66-74, 2010.

95. Dudák, M., V. Novák, P. Kočí, M. Marek, P. Blanco-García and D. Thompsett, "Impact of zeolite and γ-alumina intra-particle diffusion on the performance of a dual layer catalyst", *Chemical Engineering Journal*, Vol. 301, pp. 178-187, 2016.

96. Veser, G. and J. Frauhammer, "Modelling steady state and ignition during catalytic methane oxidation in a monolith reactor", *Chemical Engineering Science*, Vol. 55, No. 12, pp. 2271-2286, 2000.

97. Adhikari, S., S. D. Fernando and A. Haryanto, "Kinetics and reactor modeling of hydrogen production from glycerol via steam reforming process over Ni/CeO_2 catalysts", *Chemical Engineering & Technology*, Vol. 32, No. 4, pp. 541-547, 2009.

98. Koc, S. and A. K. Avci, "Reforming of glycerol to hydrogen over Ni-based catalysts in a microchannel reactor", *Fuel Processing Technology*, Vol. 156, pp. 541-547, 2009.

99. Silva, J. M., M. Soria and L. M. Madeira, "Steam reforming of glycerol for hydrogen production: Modeling study", *International Journal of Hydrogen Energy*, Vol. 41, No. 3, pp. 1408-1418, 2016.

100. Hosukoglu, M. I., M. Karakaya and A. K. Avci, "Modeling and simulation of hydrocracking of Fischer–Tropsch hydrocarbons in a catalytic microchannel reactor", *Industrial & Engineering Chemistry Research*, Vol. 51, No. 26, pp. 8913-8921, 2012.

101. Gumuslu, G. and A. K. Avci, "Parametric analysis of Fischer-tropsch synthesis in a catalytic microchannel reactor", *AIChE Journal*, Vol. 58, No. 1, pp. 227-235, 2012.

102. Hardt, S., W. Ehrfeld, V. Hessel and K. V. Bussche, "Strategies for size reduction of microreactors by heat transfer enhancement effects", *Chemical Engineering Communications*, Vol. 190, No. 4, pp. 540-559, 2003.

103. Lynch, C. T., *CRC Handbook of Materials Science: Material Composites and Refractory Materials*, CRC press, 1975.

APPENDIX A: CALIBRATION OF THE GAS CHROMATOGRAPHS

Calibration curves for N_2, H_2, CH_4 and CO gases analyzed by Shimadzu GC-2014 equipped with molecular Sieve 5A are represented in the following figures.

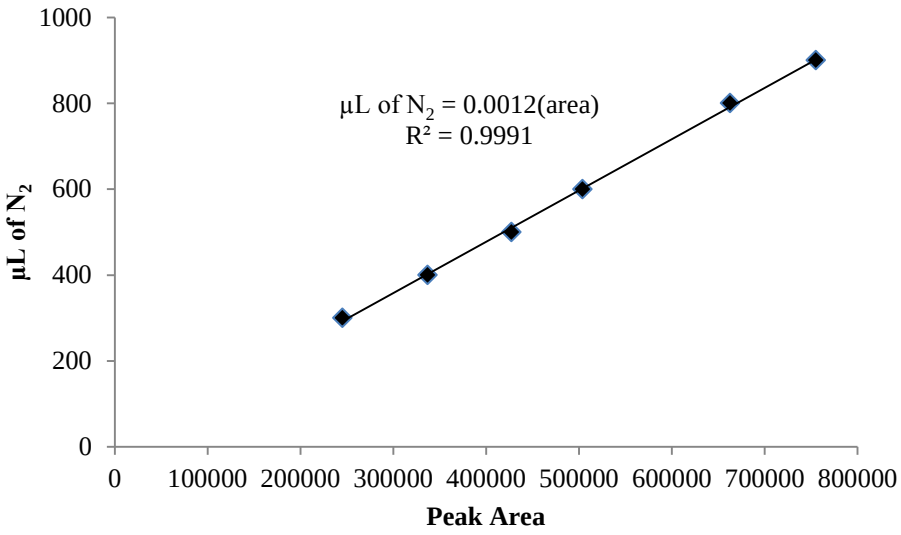

Figure A.1. Calibration Curve for N_2.

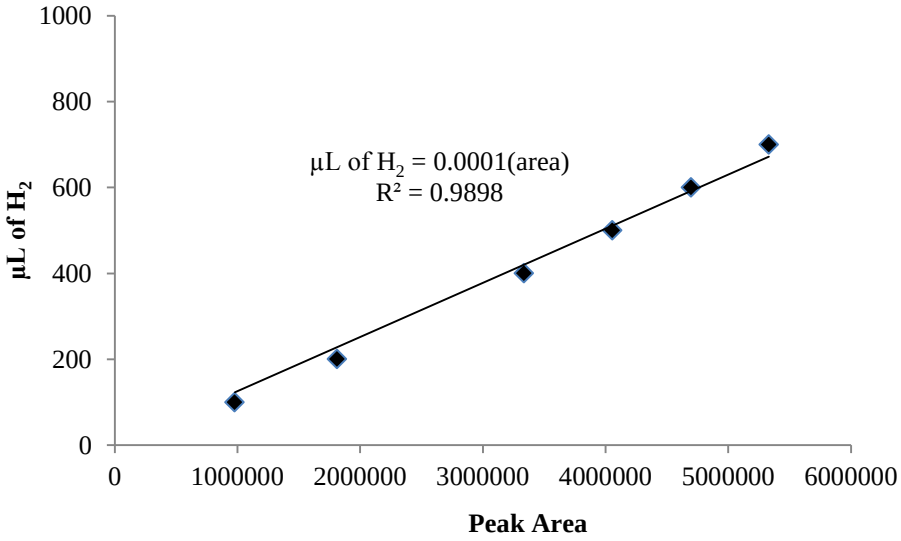

Figure A.2. Calibration Curve for H_2.

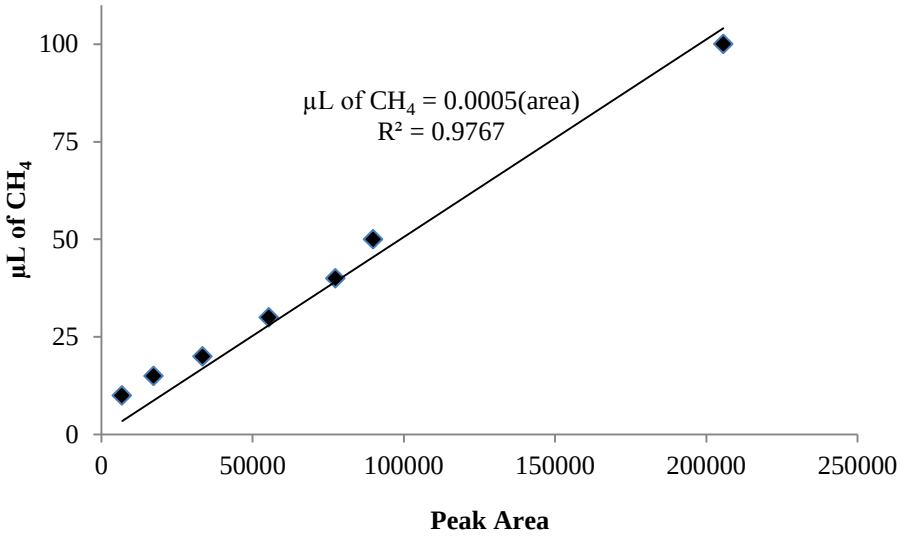

Figure A.3. Calibration Curve for CH_4.

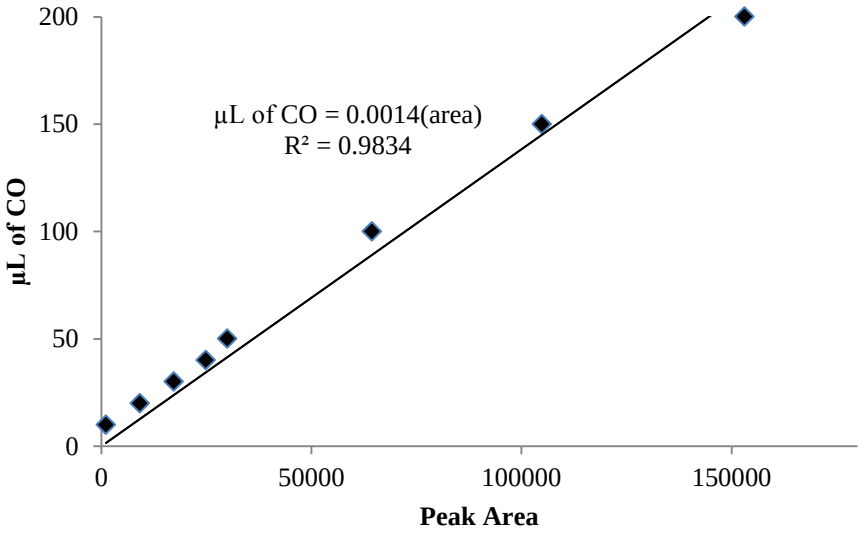

Figure A.4. Calibration Curve for CO.

Calibration curves for CO_2, C_2H_4 and C_2H_6 gases analyzed by GC-8A equipped with Porapak Q are represented in the following figures.

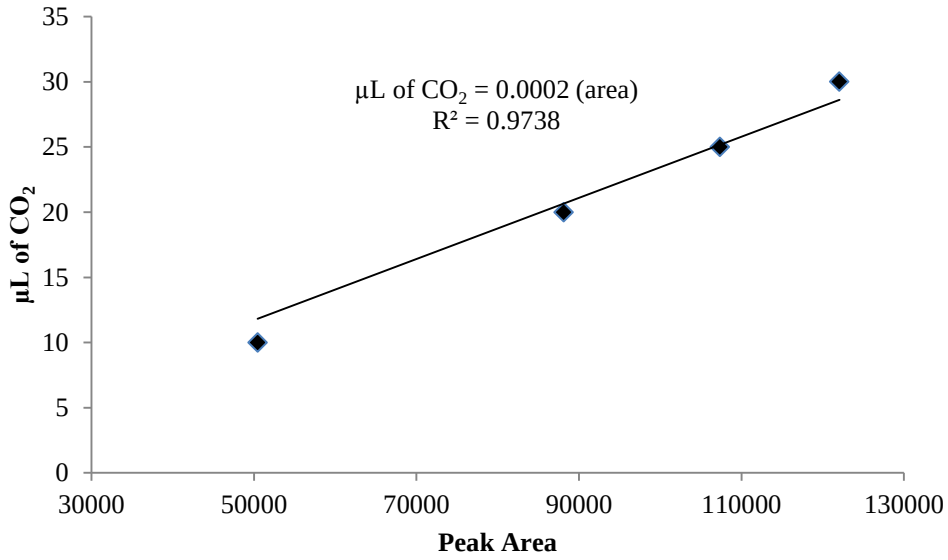

Figure A.5. Calibration Curve for CO_2.

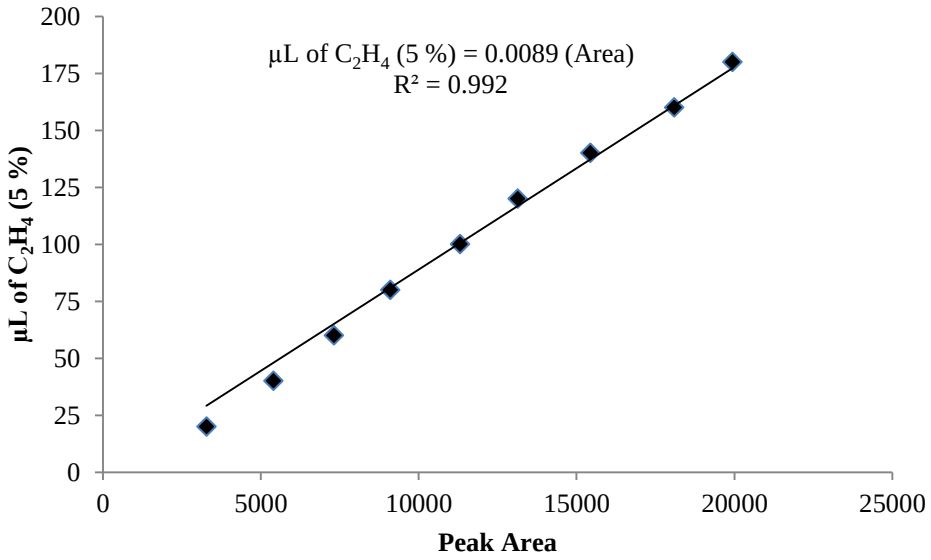

Figure A.6. Calibration Curve for C_2H_4.

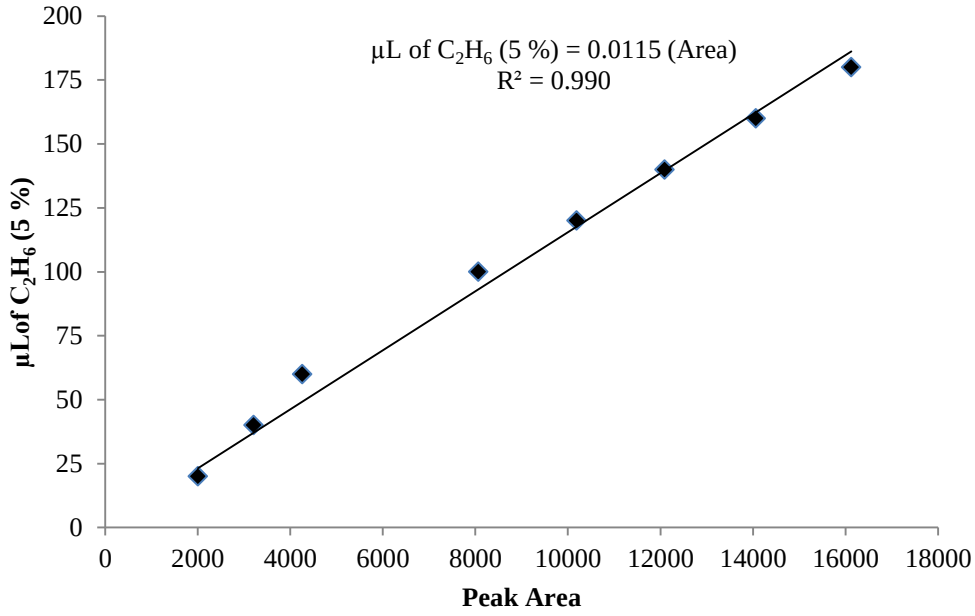

Figure A.7. Calibration Curve for C_2H_6.